

# The comptonizing medium of the black-hole X-ray binary MAXI J1535–571 through type-C quasi-periodic oscillations

Divya Rawat<sup>1\*</sup>, Mariano Méndez<sup>2</sup>, Federico García<sup>2,3,4</sup>, Diego Altamirano<sup>5</sup>, Konstantinos Karpouzas<sup>2,5</sup>, Liang Zhang<sup>5</sup>, Kevin Alabarta<sup>2,5</sup>, Tomaso M. Belloni<sup>6</sup>, Pankaj Jain<sup>7</sup>, Candela Bellavita<sup>4</sup>

<sup>1</sup>*Inter-University Center for Astronomy and Astrophysics, Ganeshkhind, Pune 411007, India*

<sup>2</sup>*Kapteyn Astronomical Institute, University of Groningen, PO BOX 800, Groningen NL-9700 AV, the Netherlands*

<sup>3</sup>*Instituto Argentino de Radioastronomía (CCT La Plata, CONICET; CICPBA; UNLP), C.C.5, (1894) Villa Elisa, Buenos Aires, Argentina*

<sup>4</sup>*Facultad de Ciencias Astronómicas y Geofísicas, Universidad Nacional de La Plata, Paseo del Bosque, B1900FWA La Plata, Argentina*

<sup>5</sup>*School of Physics and Astronomy, University of Southampton, Southampton SO17 1BJ, UK*

<sup>6</sup>*INAF-Osservatorio Astronomico di Brera, via E. Bianchi 46, I-23807, Merate, Italy*

<sup>7</sup>*Department of physics, IIT Kanpur, Kanpur, Uttar Pradesh 208016, India*

Accepted XXX. Received YYY; in original form ZZZ

## ABSTRACT

We present a detailed spectral and temporal analysis of the black-hole candidate MAXI J1535–571 using NICER observations in September and October 2017. We focus specifically on observations in the hard-intermediate state when the source shows type-C quasi-periodic oscillations (QPOs). We fitted the time-averaged spectrum of the source and the rms and phase-lag spectra of the QPO with a one-component time-dependent Comptonization model. We found that the corona contracts from  $\sim 10^4$  to  $\sim 3 \times 10^3$  km as the QPO frequency increases from  $\sim 1.8$  Hz to  $\sim 9.0$  Hz. The fits suggest that the system would consists of two coronas, a small one that dominates the time-averaged spectrum and a larger one, possibly the jet, that dominates the rms and lag spectra of the QPO. We found a significant break in the relation of the spectral parameters of the source and the properties of the QPO, including its lag spectra, with QPO frequency. The change in the relations happens when the QPO frequency crosses a critical frequency  $\nu_c \approx 3.0$  Hz. Interestingly, the QPO reaches this critical frequency simultaneously as the radio emission from the jet in this source is quenched.

**Key words:** accretion, accretion discs — black hole physics — X-rays: binaries — X-rays: individual: MAXI J1535–571

## 1 INTRODUCTION

In the outburst, the transient black-hole X-ray binary (BHXB) system shows substantial X-ray variability (Belloni & Stella 2014). These systems spend long periods in quiescence, with sporadic outbursts lasting weeks to months, during which the X-ray flux increases by up to three orders of magnitude compared to the quiescent phase (Remillard & McClintock 2006). During an outburst, transient BHXBs initially appear in the low-hard state (LHS) and, as the outburst progresses, move to the high-soft state (HSS) via the hard-intermediate (HIMS) and soft-intermediate state (SIMS) (Belloni et al. 2005, 2011, and references within). Finally, before returning to the quiescent state, BHXBs transition from the HSS to the LHS. In the LHS, a hard component due to Comptonization from an electron plasma with temperature 50 – 100 keV appears in the X-ray spectrum as a power law with photon index 1.5–2.0 (Gilfanov 2010). In contrast, the HSS spectrum is dominated by an optically thick thermal component generally modelled with a

multi-temperature disc blackbody, occasionally accompanied by a soft power-law-like component with  $\Gamma \geq 2$  (Méndez & van der Klis 1997; Done et al. 2007). The evolution of the outburst of a BHXB can be best characterised in a hardness-intensity diagram (HID), where typically systems trace a well-defined path often shaped as a “q” (Fender et al. 2004, Belloni et al. 2005).

These systems show complex fast-time variability, which is strongly state-dependent. This variability takes the form of broadband noise components on top of which, in specific states, quasi-periodic oscillations (QPOs) can be observed (e.g. Chen et al. 1997; Takizawa et al. 1997; Psaltis et al. 1999; Nowak 2000; Casella et al. 2004, 2005; Belloni et al. 2005). The QPOs appear in the power density spectrum (PDS; van der Klis & Jansen 1985) as relatively narrow peaks. The QPOs have been broadly divided into three categories, the mHz QPO with QPO frequency ranging from few mHz to Hz (e.g., Dewangan et al. 2006; Koljonen et al. 2011, Altamirano & Strohmayer 2012, Pasham et al. 2013), low-frequency QPOs (LFQPOs) with frequencies ranging from just below 1 Hz up to 20 Hz (e.g., Motta et al. 2015),

\* E-mail: rawatdivya838@gmail.com (DR)

and high-frequency QPOs (HFQPOs) with frequencies above 100 Hz and up to  $\sim 500$  Hz (e.g., Miller et al. 2001, Strohmayer 2001, Belloni et al. 2012, Méndez et al. 2013, Belloni & Stella 2014). LFQPOs appear in different spectral states and have been further classified as type A, B, and C (Wijnands et al. 1999, Homan et al. 2001, Remillard et al. 2002, Casella et al. 2004). Among the three types, type-C is the one that is most often observed, showing a high rms amplitude, between 1% and 20%, and a quality factor<sup>1</sup> usually larger than 6.0 (Wijnands et al. 1999; Casella et al. 2004; Belloni & Stella 2014, see Ingram & Motta 2019, for a review).

MAXI J1535–571 (hereafter MAXI J1535) is a galactic transient, initially detected by MAXI/GSC (Negoro et al. 2017a) and SWIFT/BAT (Kennea et al. 2017, Markwardt et al. 2017) on September 2, 2017. The X-ray variability (Negoro et al. 2017b), optical (Scaringi & ASTR211 Students 2017) and near-infrared (Dinçer 2017) properties of the source suggest that MAXI J1535 is a low-mass X-ray binary (LMXB) source. Radio observations with the Australia Telescope Compact Array (ATCA) show a signature of a compact radio jet (Russell et al. 2017); this and the observed luminosity suggest that this system harbours a black hole (Negoro et al. 2017b). Study of radio (Chauhan et al. 2019) and X-ray (Sridhar et al. 2019) observations suggest that the distance to the source is 4–6 kpc, and the jet inclination angle is constrained to  $\leq 45^\circ$  (Russell et al. 2019). X-ray spectral studies suggest that the system harbours a near-maximally spinning black hole (Gendreau et al. 2017, Xu et al. 2018, Miller et al. 2018). There are some conflicting estimates of the mass of the black hole in the system (Sreehari et al. 2019, Sridhar et al. 2019), but they are all based on fits to the X-ray spectrum and are therefore model dependent. No dynamical mass measurement from optical observations is available.

A state transition study of MAXI J1535 during outburst, from September 2017 to April 2018 (Nakahira et al. 2018) shows that the source behaved like other BHXB systems tracing a q-shape in the HID (Tao et al. 2018). In the LHS and HIMS, starting from September 9–18, 2017, MAXI J1535 showed a type-C QPO with a centroid frequency in the 0.2–3.4 Hz range (Gendreau et al. 2017, Mereminskiy et al. 2018, Stiele & Kong 2018, Huang et al. 2018, Bhargava et al. 2019). The source transitioned to the SIMS and then to the HSS from September 19–26, 2017. The stable and weak type A/B LFQPO appears in the SIMS (Stiele & Kong 2018, Stevens et al. 2018, Huang et al. 2018). In the HIMS and LHS, the type-C QPO reappears from September 26 to October 9, 2017. After the end of the main outburst in mid-May 2018, five re-brightening events were reported by Parikh et al. (2019). A state transition during these re-flares was reported by Cúneo et al. (2020) using NICER observations.

Kumar & Misra (2014) proposed a model to study the Comptonisation medium of neutron-star X-ray binary sys-

tems, which was later extended by Karpouzas et al. (2020). This model was originally developed for high-frequency QPOs in accreting neutron-star systems. Still, it has been recently extended by Bellavita et al. (2022) to LFQPOs in BHXBs and was applied to the type-C QPO in GRS 1915+105 by Karpouzas et al. (2021) and Méndez et al. (2022), and the type-B QPO in MAXI J1348–630 (García et al. 2021; Bellavita et al. 2022). Zhang et al. (2022) has applied the same model using Insight-HXMT observations of the type-C QPO in MAXI J1535 up to 150 keV. The rationale behind applying this model to type-C in BHXB is that the fractional rms amplitude of these QPOs can be as large as  $\sim 15\%$  up to  $\sim 200$  keV (Ma et al. 2021). At those energies, Comptonization dominates the emission in these systems (e.g., the disc and the reflection component peak at, respectively,  $\sim 1$ –3 keV and  $\sim 20$ –25 keV and both drop quickly above that), and hence Comptonization is most likely responsible for the rms amplitude and lags of the QPO.

In this paper, we report the results of the spectro-temporal analysis of MAXI J1535 using NICER observations. To study the Comptonization medium of the source, we fit the rms and phase-lag spectra of the QPO with a one-component time-dependent Comptonization model, VKOMPTHDK (Karpouzas et al. 2020; Bellavita et al. 2022). In Section 2, we describe the observations and data analysis techniques, and in Section 3 we present the results of our analysis and the fits of the model to the rms and lag spectra of the type-C QPO. Finally, we discuss our findings in Section 4 and summarise our results in Section 5.

## 2 OBSERVATION AND DATA ANALYSIS

We used observations of MAXI J1535 obtained in September and October 2017 with the Neutron Star Interior Composition Explorer (NICER Gendreau et al. 2012). The observations ID’s used are 1050360101–1050360120 & 1130360101–1130360114. NICER’s XTI (X-ray Timing Instrument Gendreau et al. 2016) covers the 0.2–12.0 keV band and has an effective area of  $>2000$  cm<sup>2</sup> at 1.5 keV. The energy and time resolutions are 85 eV at 1 keV and  $4 \times 10^{-8}$  s (hereafter  $\Delta t_{\text{nicer}}$ ), respectively. We used the NICERL2<sup>2</sup> task to process each observation applying the standard calibration process and screening. We used only those intervals for which the exposure time was  $> 100$  s after running the NICERL2 task. For some intervals, we found that the source flux was varying significantly. To make sure we are not averaging features of two spectrally and temporally different states, we divided a single observation into segments with a more or less constant source count rate and studied the temporal and spectral properties of each segment independently. The details of each observation and segment are given in Table 1.

### 2.1 Timing analysis

We extracted the fractional rms amplitude (root-mean square) normalised (Belloni & Hasinger 1990) PDS for each

<sup>1</sup> Quality factor=QPO frequency/QPO width

<sup>2</sup> [https://heasarc.gsfc.nasa.gov/docs/nicer/analysis\\_threads/nicerl2/](https://heasarc.gsfc.nasa.gov/docs/nicer/analysis_threads/nicerl2/)

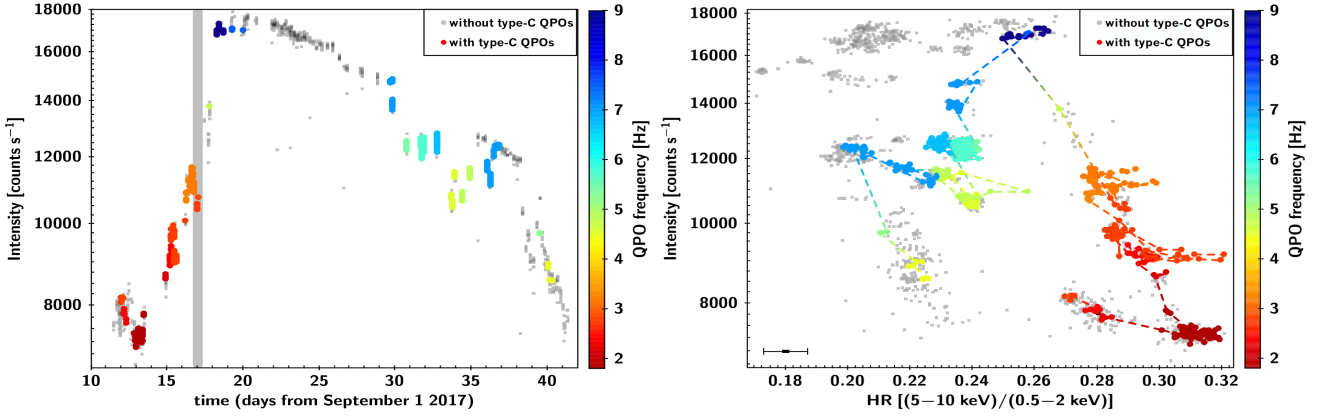


**Figure 1.** Left panel: NICER light curve of MAXI J1535–571 in the 0.5–10.0 keV band. The shaded area represents the approximate time when the radio emission was quenched (Russell et al. 2019). Right panel: Hardness intensity diagram (HID) using NICER observations. In the HID, the line shows the general movement of the source in this diagram as the outburst progressed, with the start and end points of the outburst at, (HR = 0.27, Intensity = 8000) and (HR = 0.22, Intensity = 8000), respectively. In both panels, each point corresponds to 100 sec, and the colour scale panels indicate the frequency of the QPO.

**Table 1.** Observation log of MAXI J1535, including timing parameters. The columns are the observation number, the NICER ObsID, the start and end time of the observation, the 0.5–10.0 keV count rate, the standard deviation of the count rate,  $\sigma_{count}$ , the hardness ratio, HR, the standard deviation of the hardness ratio,  $\sigma_{HR}$ , the QPO centroid frequency and the QPO fractional rms amplitude. The errors are at  $1\sigma$ . The observations with an asterisk are those for which the QPO was insignificant in the lowest energy bands.

Obs no.	ObsID	Tstart (M.J.D)	Tstop (M.J.D)	count rate (0.5–10.0 keV)	$\sigma_{count}$	HR $\frac{(5-10\text{keV})}{(0.5-2.0\text{keV})}$	$\sigma_{HR}$	QPO frequency (Hz)	QPO Fractional rms (%)
1	1050360105	58008.988	58009.126	8140 ± 5	48	0.272	0.002	2.74 ± 0.01	7.0 ± 0.2
2	1050360105	58009.165	58009.193	7847 ± 4	36	0.280	0.002	2.44 ± 0.01	6.5 ± 0.2
3	1050360105	58009.229	58009.301	7676 ± 6	30	0.285	0.004	2.32 ± 0.01	6.7 ± 0.2
4	1050360105	58009.807	58009.945	7327 ± 4	65	0.307	0.003	1.83 ± 0.01	7.3 ± 0.2
5	1050360106	58010.001	58010.525	7364 ± 1	138	0.311	0.005	1.81 ± 0.00	7.2 ± 0.1
6	1050360107	58011.865	58011.940	8654 ± 7	47	0.299	0.002	2.15 ± 0.01	6.9 ± 0.2
7	1050360108	58012.187	58012.258	9134 ± 3	130	0.294	0.006	2.41 ± 0.01	7.4 ± 0.2
8	1050360108	58012.316	58012.583	9492 ± 2	320	0.285	0.002	2.77 ± 0.01	7.3 ± 0.2
9	1050360109	58013.216	58013.222	10088 ± 1	4	0.285	0.004	2.75 ± 0.02	7.0 ± 0.2
10	1050360109	58013.281	58013.410	10922 ± 4	191	0.275	0.008	3.27 ± 0.02	7.0 ± 0.3
11	1050360109	58013.481	58013.740	11290 ± 2	227	0.282	0.005	3.19 ± 0.03	6.7 ± 0.3
12	1050360109	58013.988	58013.998	10461 ± 5	71	0.288	0.001	2.72 ± 0.01	6.7 ± 0.2
13	1050360110	58014.053	58014.063	10744 ± 1	5	0.286	0.002	2.84 ± 0.01	7.5 ± 0.2
14	1050360110	58014.824	58014.835	13795 ± 1	5	0.269	0.003	4.75 ± 0.01	5.7 ± 0.1
15	1050360111	58015.276	58015.669	16992 ± 3	161	0.257	0.005	9.01 ± 0.04	1.7 ± 0.1
16	*1050360112	58016.240	58016.957	17040 ± 9	31	0.256	0.010	7.55 ± 0.06	2.6 ± 0.2
17	1050360113	58017.011	58017.858	16995 ± 1	7	0.244	0.017	7.45 ± 0.03	2.9 ± 0.1
18	*1130360103	58026.726	58026.814	14304 ± 2	445	0.235	0.002	7.09 ± 0.03	2.4 ± 0.1
19	1130360104	58027.755	58027.779	12363 ± 3	105	0.240	0.002	5.42 ± 0.01	4.7 ± 0.1
20	1130360105	58028.720	58028.872	12321 ± 2	213	0.237	0.002	5.73 ± 0.01	4.5 ± 0.0
21	*1130360106	58029.749	58029.836	12527 ± 2	151	0.229	0.002	6.77 ± 0.02	3.5 ± 0.1
22	1130360107	58030.715	58030.865	10831 ± 2	381	0.238	0.004	4.57 ± 0.01	4.6 ± 0.1
23	1130360108	58031.361	58031.894	11163 ± 2	370	0.234	0.006	4.82 ± 0.01	3.5 ± 0.0
24	1130360113	58036.498	58036.695	9747 ± 10	19	0.206	0.007	5.19 ± 0.03	3.0 ± 0.2
25	1130360114	58037.032	58037.677	8767 ± 4	183	0.224	0.004	4.50 ± 0.01	5.0 ± 0.1

segment using the General High-energy Aperiodic Timing Software (GHATS)<sup>3</sup> version 2.1.0. The 0.2–10.0 keV data were re-binned in time by a factor of 62500, such that the time resolution was 0.0025 s, corresponding to a Nyquist frequency of 200 Hz, and PDS were produced from intervals

of 8192 points (20.48 s). For each segment, the PDS for the intervals were averaged. We fitted the PDS in the frequency 100–200 Hz, where the source shows no intrinsic variability, with a constant representing the Poisson noise, which we then subtracted. We ended up with an averaged, Poisson-noise subtracted PDS for each segment that we re-binned logarithmically such that each frequency bin is larger than the previous one by a factor  $\exp(1/100)$ . We

<sup>3</sup> [http://www.brera.inaf.it/utenti/belloni/GHATS\\_Package/Home.html](http://www.brera.inaf.it/utenti/belloni/GHATS_Package/Home.html)

**Table 2.** Time-averaged spectra and corona model parameters of MAXI J1535. The columns are the observation number, the hydrogen column density,  $N_{\text{H}}$ , the power-law photon index of NTHCOMP,  $\Gamma$ , the inner disc temperature,  $kT_{\text{in}}$ , the seed photon temperature of VKOMPTDK,  $kT_s$ , the size of the corona,  $L$ , the fraction of the flux of the seed-photon source due to feedback from the corona,  $\eta$ , and the amplitude of the variability of the external heating rate,  $\delta\dot{H}_{\text{ext}}$ . The errors are at  $1\sigma$ . The observations with an asterisk are those for which the QPO was insignificant in the lowest energy bands.

Obs no.	$N_{\text{H}}$ $10^{22} \text{ cm}^{-2}$	$\Gamma$	$kT_{\text{in}}$ (keV)	$kT_s$ (keV)	$L$ ( $10^3 \text{ km}$ )	$\eta$	$\delta\dot{H}_{\text{ext}}$ %	$\chi^2_{\nu}(\text{dof})$
1	$2.19 \pm 0.01$	$2.43 \pm 0.02$	$0.68 \pm 0.01$	$0.35 \pm 0.05$	$5.1 \pm 1.0$	$0.62 \pm 0.05$	$12.2 \pm 0.6$	231.4 (243)
2	$2.19 \pm 0.01$	$2.29 \pm 0.01$	$0.62 \pm 0.01$	$0.29 \pm 0.03$	$8.3 \pm 1.1$	$0.75 \pm 0.09$	$12.0 \pm 0.5$	191.9 (242)
3	$2.18 \pm 0.01$	$2.26 \pm 0.01$	$0.61 \pm 0.01$	$0.23 \pm 0.04$	$8.7 \pm 1.1$	$0.82^{+0.18}_{-0.38}$	$11.3 \pm 1.1$	240.5 (243)
4	$2.17 \pm 0.01$	$2.12 \pm 0.01$	$0.55 \pm 0.01$	$0.14 \pm 0.01$	$12.6 \pm 0.5$	$1.00 - 0.04$	$11.1 \pm 0.4$	219.8 (243)
5	$2.16 \pm 0.01$	$2.11 \pm 0.00$	$0.55 \pm 0.01$	$0.15 \pm 0.01$	$13.2 \pm 0.4$	$1.00 - 0.45$	$11.5 \pm 0.3$	242.3 (243)
6	$2.15 \pm 0.01$	$2.18 \pm 0.01$	$0.60 \pm 0.01$	$0.24 \pm 0.03$	$9.1 \pm 1.0$	$0.79 \pm 0.12$	$12.2 \pm 0.7$	177.9 (243)
7	$2.17 \pm 0.01$	$2.27 \pm 0.01$	$0.64 \pm 0.01$	$0.36 \pm 0.05$	$6.6 \pm 1.2$	$0.64 \pm 0.07$	$15.0 \pm 0.7$	173.2 (243)
8	$2.15 \pm 0.01$	$2.67 \pm 0.04$	$0.79 \pm 0.01$	$0.33 \pm 0.04$	$5.7 \pm 0.9$	$0.76 \pm 0.07$	$11.2 \pm 0.7$	234.8 (243)
9	$2.19 \pm 0.01$	$2.34 \pm 0.02$	$0.68 \pm 0.01$	$0.47 \pm 0.07$	$4.8 \pm 0.9$	$0.59 \pm 0.05$	$14.4 \pm 0.9$	169.3 (243)
10	$2.21 \pm 0.01$	$2.48 \pm 0.02$	$0.74 \pm 0.01$	$0.39 \pm 0.07$	$4.4 \pm 1.2$	$0.55 \pm 0.07$	$13.5 \pm 1.0$	155.1 (243)
11	$2.19 \pm 0.01$	$2.85 \pm 0.11$	$0.85 \pm 0.02$	$0.36 \pm 0.05$	$5.5 \pm 1.2$	$0.77 \pm 0.11$	$10.5 \pm 0.9$	192.2 (222)
12	$2.20 \pm 0.01$	$2.33 \pm 0.01$	$0.67 \pm 0.01$	$0.37 \pm 0.04$	$6.5 \pm 0.8$	$0.66 \pm 0.05$	$13.3 \pm 0.5$	152.4 (243)
13	$2.20 \pm 0.01$	$2.36 \pm 0.01$	$0.69 \pm 0.01$	$0.37 \pm 0.04$	$6.4 \pm 0.8$	$0.69 \pm 0.06$	$14.3 \pm 0.5$	176.3 (243)
14	$2.23 \pm 0.01$	$2.61 \pm 0.06$	$0.98 \pm 0.02$	$0.43 \pm 0.05$	$3.8 \pm 0.5$	$0.73 \pm 0.06$	$14.1 \pm 0.8$	168.4 (242)
15	$2.30 \pm 0.01$	$2.49 \pm 0.17$	$1.18 \pm 0.01$	$0.56 \pm 0.04$	$4.0 \pm 0.5$	$1.00 - 0.11$	$17.3 \pm 2.0$	195.8 (239)
16	$2.29 \pm 0.01$	$2.60 \pm 0.14$	$1.13 \pm 0.02$	$0.52 \pm 0.07$	$3.7 \pm 1.0$	$0.69 \pm 0.18$	$15.6 \pm 2.4$	165.0 (236)
17	$2.29 \pm 0.00$	$2.40 \pm 0.24$	$1.19 \pm 0.01$	$0.39 \pm 0.04$	$3.4 \pm 0.2$	$0.88 \pm 0.04$	$20.6 \pm 1.2$	177.0 (242)
18	$2.27 \pm 0.01$	$2.71 \pm 0.10$	$1.05 \pm 0.02$	$0.55 \pm 0.04$	$3.0 \pm 0.3$	$0.60 \pm 0.06$	$11.7 \pm 0.8$	244.4 (229)
19	$2.24 \pm 0.00$	$2.61 \pm 0.08$	$0.95 \pm 0.02$	$0.46 \pm 0.04$	$3.8 \pm 0.5$	$0.65 \pm 0.05$	$14.3 \pm 1.1$	203.6 (242)
20	$2.30 \pm 0.01$	$3.03 \pm 0.02$	$0.85 \pm 0.01$	$0.63 \pm 0.02$	$4.0 \pm 0.2$	$0.57 \pm 0.03$	$14.1 \pm 0.4$	204.5 (240)
21	$2.31 \pm 0.01$	$3.38 \pm 0.05$	$0.92 \pm 0.01$	$0.76 \pm 0.04$	$2.7 \pm 0.2$	$0.44 \pm 0.03$	$13.5 \pm 0.8$	198.2 (215)
22	$2.31 \pm 0.02$	$2.66 \pm 0.03$	$0.71 \pm 0.02$	$0.57 \pm 0.03$	$4.8 \pm 0.4$	$0.51 \pm 0.04$	$13.3 \pm 0.6$	258.0 (219)
23	$2.28 \pm 0.01$	$3.07 \pm 0.04$	$0.85 \pm 0.01$	$0.55 \pm 0.03$	$4.5 \pm 0.4$	$0.66 \pm 0.05$	$9.1 \pm 0.5$	223.1 (238)
24	$2.21 \pm 0.00$	$2.69 \pm 0.08$	$0.96 \pm 0.02$	$0.40 \pm 0.05$	$6.2 \pm 1.5$	$1.00 - 0.33$	$12.8 \pm 1.9$	191.4 (241)
25	$2.23 \pm 0.00$	$2.58 \pm 0.03$	$0.82 \pm 0.02$	$0.43 \pm 0.03$	$5.5 \pm 0.7$	$0.67 \pm 0.08$	$15.9 \pm 0.5$	174.9 (242)

fitted all the PDS with a model consisting of up to five Lorentzians to represent the broadband noise component and the QPOs. Each Lorentzian has three parameters: the centroid frequency,  $\nu_0$ , the full-width at half-maximum, FWHM, and the total power, equal to the integral of the Lorentzian function over the full frequency range. We only included a Lorentzian in the model if its total power was at least  $3\sigma$  different from zero, given the error of this parameter. We visually inspected the PDS from all segments and used only those with a clear type-C QPO.

Next, we extracted PDS in 10 energy bands, 1.0–1.5, 1.5–1.9, 1.9–2.3, 2.3–3.0, 3.0–3.5, 3.5–4.0, 4.0–5.0, 5.0–6.0, 6.0–8.0, and 8.0–12.0 keV that we normalised to fractional rms for each band. To extract phase/time lags, we computed FFTs from the data in the ten energy bands and measured the lags using the phases of the cross-spectra with the 2.0–3.0 keV band as a reference, following the procedure of Nowak et al. (1999b). To calculate the lags of the QPO, we averaged the cross spectra within one full-width half-maximum around the centroid frequency of the QPO for each segment in which we detected a significant QPO. For 4 segments, marked with an asterisk in Table 1, the QPO was insignificant in the lowest energy bands. We merged some low-energy bands in those cases and extracted the rms and lag spectra for 7 energy bands (1.0–2.3, 2.3–3.5, 3.5–4.0, 4.0–5.0, 5.0–6.0, 6.0–8.0, and 8.0–12.0 keV).

## 2.2 Spectral analysis

We produced the spectra and background files using the NICER background estimator tool 3C\_50\_RGv5<sup>4</sup>. The background-subtracted spectrum for each segment was re-binned using GRPPHA such that each spectral bin had at least 30 counts and the bins over-sampled the spectral resolution of the detector by a factor 3. We used HEASOFT version 6.30 and CALDB version 20210707 to create the response (rmf) and ancillary response (arf) files. We fitted the time-averaged spectrum of the source in the 1.0 – 10.0 keV band using the model TBABS\*(DISKBB+GAUSS+NTHCOMP) in XSPEC. The TBABS models the interstellar absorption. We used the cross-section tables of Verner et al. (1996) and the abundances of Wilms et al. (2000) and left the hydrogen column density as a free parameter. The DISKBB component models the thermal emission from an optically thick and geometrically thin accretion disc (Mitsuda et al. 1984, Makishima et al. 1986) while NTHCOMP (Zdziarski et al. 1996, Życki et al. 1999) models the Comptonised emission from the X-ray corona. We kept both the DISKBB parameters, the temperature at inner disk radius,  $kT_{\text{in}}$ , and the normalisation free. The NTHCOMP model parameters are the power-law photon index,  $\Gamma$ , electron temperature,  $kT_e$ , seed photon temperature,  $kT_{\text{bb}}$ , and normalization.

<sup>4</sup> [https://heasarc.gsfc.nasa.gov/docs/nicer/tools/nicer\\_bkg\\_est\\_tools.html](https://heasarc.gsfc.nasa.gov/docs/nicer/tools/nicer_bkg_est_tools.html)



The seed-photon temperature  $kT_{bb}$  was tied to  $kT_{in}$  of the DISKBB component. We have fitted a relatively broad iron line present in the residuals with a Gaussian, GAUSS in XSPEC. In addition to the broad line, the spectra show narrow residuals at  $\sim 6.4$  keV. We have added one more GAUSS component to account for the narrow line (if required).

We fit the rms with the model VKOMPTHDK\*DILUTION<sup>5</sup> (Karpouzas et al. 2020; Bellavita et al. 2022) and the lag spectra with the model VKOMPTHDK at the QPO frequency. VKOMPTHDK can compute both the time-dependent and the time-averaged spectrum. The time-dependent version of VKOMPTHDK is the one that fits the rms and lags. The time-averaged version of VKOMPTHDK is the same as NTHCOMP. The parameters of VKOMPTHDK are hence the temperature of the seed photon source,  $kT_s$ , the temperature of the corona,  $kT_e$ , the power-law index,  $\Gamma$  (all of them identical to  $kT_{bb}$ ,  $kT_e$  and  $\Gamma$  of NTHCOMP), plus the size of the corona,  $L$ , the feedback fraction,  $\eta$  (between 0 to 1), the amplitude of the variability of the external heating rate,  $\delta\dot{H}_{ext}$ , and the lag of the model in the 2–3 keV energy band,  $reflag$ . These parameters can be used to compute the fraction of the corona flux,  $\eta_{int}$ , that returns to the disc (see Karpouzas et al. 2020 for details). The parameters  $L$ ,  $\eta$ ,  $\delta\dot{H}_{ext}$ , and  $reflag$  are only relevant for the fits to the rms and lag spectra and do not affect the time-averaged version of the VKOMPTHDK. The parameter  $reflag$  is an additive normalisation that allows the model to match the data, given that the observer is free to choose the reference energy band of the lags. We froze the electron temperature of NTHCOMP and VKOMPTHDK at  $kT_e = 21$  keV (Sridhar et al. 2019) because the 1.0–10.0 keV energy band is not suitable to constrain it. The DILUTION component is a function of energy ( $E$ ). It accounts for the fact that the rms amplitude we observe is diluted by the emission of the other components that we assume do not vary. The DILUTION component is therefore defined as;

$$\text{dilution}(E) = \frac{\text{nthcomp}(E)}{\text{diskbb}(E) + \text{gauss}(E) + \text{nthcomp}(E)}$$

(See details in Bellavita et al. (2022).) Because  $N_H$  towards the source is high, any emission below 1 keV could be attributed to calibration artefacts; therefore, we have decided to exclude data below 1.0 keV in our fits. Using HXMT data in the 2–100 keV range, Zhang et al. (2022) reported a hydrogen column density,  $N_H = 5.6 \times 10^{22} \text{ cm}^{-2}$ , that is higher than the value we have obtained here using NICER in the 1–10 keV range.

### 3 RESULTS

The left panel of Figure 1 shows the NICER light curve of MAXI J1535 during its 2017 outburst. While the right panel of Figure 1 shows the evolution of the source in the HID. Here intensity is defined as the source count rate in the 0.5–10.0 keV band, and hardness ratio (HR) is the ratio of the source intensity in the 5.0–10.0 keV and 0.5–2.0 keV bands. The colour scale shown at the right of both Figures represents the QPO frequency range 1.8–9.0 Hz, with red

being the lowest and navy blue being the highest end of the QPO frequency range. The source’s X-ray count rate and HR and their respective standard deviation values for each segment are given in Table 1.

#### 3.1 Spectral fits

From the fits to the time-averaged spectrum, the rms and phase-lag spectra of the QPO for each segment, we find that during the first two days of our observations, the inner disc temperature,  $kT_{in}$ , and the photon index,  $\Gamma$ , of the Comptonised component first drop (Figure 2) as the source moves to the right in the HID (Figure 1 right panel), from hardness ratio  $\sim 0.27$  to hardness ratio  $\sim 0.31$ . Between MJD 58010 and MJD 58012, the source intensity increases, and the spectrum softens again. The source starts to move up and to the left in the HID, and  $kT_{in}$  and  $\Gamma$  increase very quickly for about five days. At the end of this period, the source reaches the highest intensity in our observations. The accretion disc is the hottest,  $kT_{in} \approx 1.1 - 1.2$  keV, and the Comptonised component is described with  $\Gamma \approx 2.7 - 2.8$ . At this point, the source enters the HSS and the PDS show no QPOs. When the source transitions back to the SIMS and the HIMS, at around MJD 58025,  $kT_{in}$  and  $\Gamma$  are approximately correlated with the X-ray flux (see Figures 1 and 2). We give each segment’s spectral parameters and goodness of fit in Table 2. In a few segments the reduced  $\chi^2$  is less than 1 (last column of Table 2). The low  $\chi^2$  values come from the fit to the steady-state spectra (SSS). We provide the  $\chi^2$  and the number of channels for the fits to the individual spectra and the total  $\chi^2$  and the number of degree of freedom in Table A.1. Unless otherwise specified, the errors represent the  $1\sigma$  confidence (68%) interval for the corresponding parameter.

#### 3.2 Power Density Spectra

Following Belloni et al. (2002), we fit the PDS with a 0-centred Lorentzian to represent the broadband noise component and three separate Lorentzians to fit the narrow QPO, its harmonic component, and the high-frequency noise. The features in the PDS have a frequency in the ratio of 1:2, and we, therefore, identify the strongest peak as the fundamental and the other as the second harmonic. The PDS also shows a low-frequency noise component when the strongest QPO peak was at a frequency above 4.0 Hz (Figure 3). Therefore, we used an additional Lorentzian to fit the low-frequency noise component whenever required.

We have studied the QPO fractional rms amplitude in the 0.5–10.0 keV energy band as a function of QPO frequency (left panel of Figure 4) and confirmed that the QPO we have identified as fundamental followed a similar relation to the one found for GRS 1915+105 (Zhang et al. 2020). The type-C QPO appears in the LHS and HIMS as a narrow peak with high rms amplitude in the PDS. The properties of the observed broadband noise and the QPO justify the identification of the QPO as type-C (Casella et al. 2004). We fitted the PDS for three different energy bands (0.5–2.0 KeV, 2.0–4.0 keV, 4.0–10.0 keV) when the type-C QPO was at 1.8 Hz, 4.5 Hz, and 7.0 Hz. We show the fitted PDS and their respective frequency lag spectra in Figure 3. The lag

<sup>5</sup> <https://github.com/candebellavita/vkompthd>

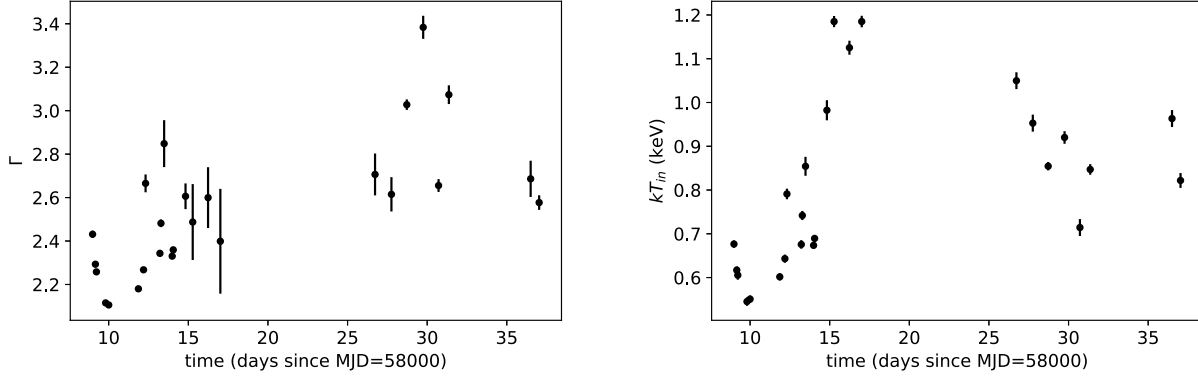


**Figure 2.** The evolution of  $\Gamma$  of the corona (left panel) and  $kT_{in}$  of the disc (right panel) of MAXI J1535–571. The values of  $\Gamma$  and  $kT_{in}$  are obtained from the fits to the time-averaged spectra, the rms and phase-lag spectra of the QPO.

and rms values at the QPO frequency are given in Appendix Table A.2. When the QPO frequency is higher than 7.0 Hz, the QPO fractional rms amplitude decreases, and the harmonic component becomes insignificant.

The evolution of the QPO centroid frequency is shown in the right panel of Figure 4. The QPO frequency first decreases from 2.7 to 1.8 Hz and then increases to its maximum value of 9.0 Hz. After that, the QPO frequency varies in the 4.5 – 7.5 Hz range. The QPO frequency and fractional rms amplitude in the 0.5 – 10.0 keV band for each observation are given in Table 1. We have plotted  $\Gamma$  and  $kT_{in}$  as a function of QPO frequency as shown in Figure 5. We found that both  $\Gamma$  and  $kT_{in}$  increase with QPO frequency.

To extract the rms spectrum, we fit the PDS in 10 energy bands, fixing the QPO centroid frequency and FWHM to the best-fitting values in the 2.0–10.0 keV PDS. The rms and phase lag spectra when the QPO frequency was 1.8 Hz, 4.5 Hz, and 7.0 Hz are shown in the top and bottom panels of Appendix Figure A1. While the fractional rms amplitude of the QPO increases with photon energy for all QPO frequencies, the rms spectrum steepens as the QPO frequency increases from 1.8 Hz to 7.0 Hz (see upper panels in Appendix Figure A1). The change of the slope of the rms spectrum of the QPO is driven by a factor  $\sim 3$  drop of the rms amplitude at the lowest energies when the QPO is at low frequencies. In contrast, the rms amplitude at the highest energies remains more or less constant as the QPO frequency changes by a factor of  $\sim 4$ . Although, in general, the low-energy photons at the QPO frequency lag behind the high-energy photons for all QPO frequencies, the lag spectrum of the QPO changes with QPO frequency. When the QPO frequency is between 1.8 Hz and 2.4 Hz, the lag spectrum shows a minimum at  $\sim 4$  keV, with the photons at low and high energies lagging the 4–5 keV photons by 0.1 – 0.3 rad. As the QPO frequency increases, the minimum of the lag spectrum of the QPO moves to higher energies, with the minimum reaching  $\sim 9 - 10$  keV at the highest QPO frequency, and the low-energy photons lag the high-energy ones by up to  $\sim 0.8$  rad. The rms and phase-lag spectra of the QPO in MAXI J1535 in these observations with NICER are consistent with the pattern observed for the type-C QPO by Rawat et al. (2019) in GRS 1915+105

and Garg et al. (2022) in MAXI J1535 with AstroSat, over the common energy range of both instruments.

### 3.3 One component time-dependent Comptonization model

To understand the changes observed in the rms and lag spectra of the QPO (see Section 3.2), we fitted the rms and lag spectra of the QPO at each QPO frequency with the VKOMPTHDK model. During the fits we linked  $kT_e$  and  $\Gamma$  of NTHCOMP to  $kT_e$  and  $\Gamma$  of VKOMPTHDK. We first linked  $kT_s$  of VKOMPTHDK to  $kT_{in}$  of DISKBB, and we found large residuals in the fits of the phase-lag spectra (Figure 6) because VKOMPTHDK fails to reproduce the minimum of the lags. We subsequently let  $kT_{in}$  and  $kT_s$  vary independently, and the fits improve significantly (Figure 6). The simultaneous fitted time-averaged spectra, rms spectra and lag spectra when the QPO frequency was  $\sim 1.8$  Hz and the residuals of the best-fitting model are shown in Figure 7 (The peak in the residuals of the time-averaged spectra at 1.84 keV corresponds to the absorption edge features of silicon.). We show a similar plot for the QPO frequencies 4.5 Hz and 7.0 Hz (for which we show a PDS in Figure 3) in the Appendix Figures A2 and A3. We discuss the implication of letting  $kT_{in}$  and  $kT_s$  free in Section 4.3. The best-fitting parameters and  $\chi^2$  of the fits are given in Table 2.

We plotted the model parameters as a function of QPO frequency in Figure 8. The size of the corona decreases from  $\sim 10^4$  km (which corresponds to 670  $R_g$  for a 10  $M_\odot$  black hole) to  $\sim 3 \times 10^3$  km (201  $R_g$ ) while the temperature of the seed photon source,  $kT_s$ , increases from  $\sim 0.1$  keV to  $\sim 0.4$  keV as the QPO frequency increases from 1.8 Hz to  $\sim 3.0$  Hz. At QPO frequencies  $\geq 3.0$  Hz, the size of the corona and the temperature of the seed photon source remain more or less constant at respectively  $\sim 3 - 6 \times 10^3$  km and 0.5 keV. The error bars on  $\eta$  are large, and it is hard to follow any trend if present, although  $\eta$  appears to decrease from  $\sim 0.8$  to  $\sim 0.6$  as the QPO frequency increases as shown in Appendix Figure A4. The best-fitting values of  $\eta$  imply that  $\eta_{int}$  is in the range of 10–25%. Comparing the trends in Figures 5 and 8, it is apparent that there is a sudden change of the properties of the source when the QPO frequency is below and above  $\sim 3.0$  Hz. The change of behaviour of all the quantities appears to occur at the same QPO frequency, which we call critical fre-

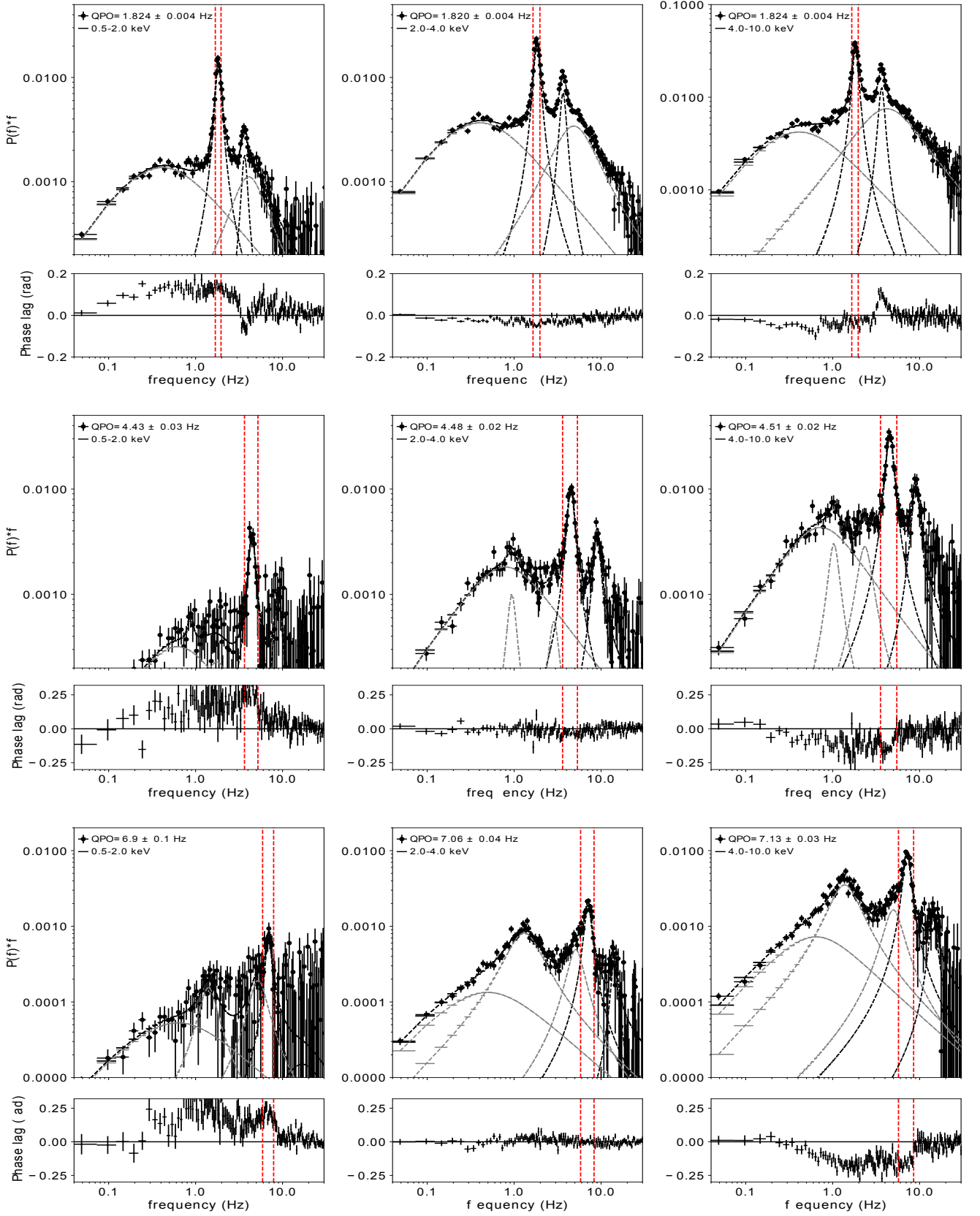


**Figure 3.** The top panels show the power density spectra (power multiplied by frequency) of MAXI J1535–571 for three QPO frequencies, 1.8 Hz, 4.5 Hz, and 7.0 Hz, and three different energy bands. The PDS is fitted with three to five Lorentzians. The bottom panels show the frequency phase-lag spectra. The reference energy band is 0.5–10.0 keV here. The vertical dashed lines indicate the ranges over which the QPO fundamental lags we measured ( $\nu \pm \text{FWHM}/2$ ).

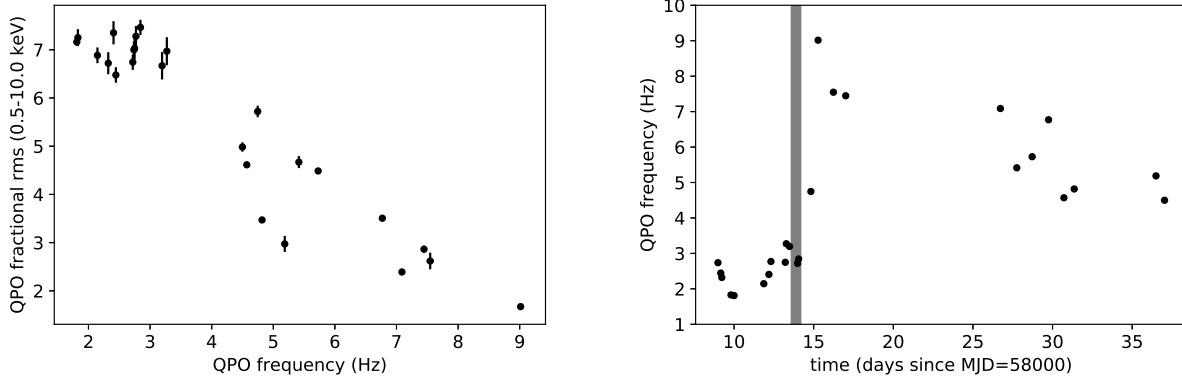


**Figure 4.** Left panel: QPO fractional rms amplitude in the 0.5–10.0 keV energy band as a function of QPO frequency for MAXI J1535–571. Right panel: Evolution of the QPO frequency of MAXI 1535–571. The shaded area represents the radio jet quenching interval (Russell et al. 2019).

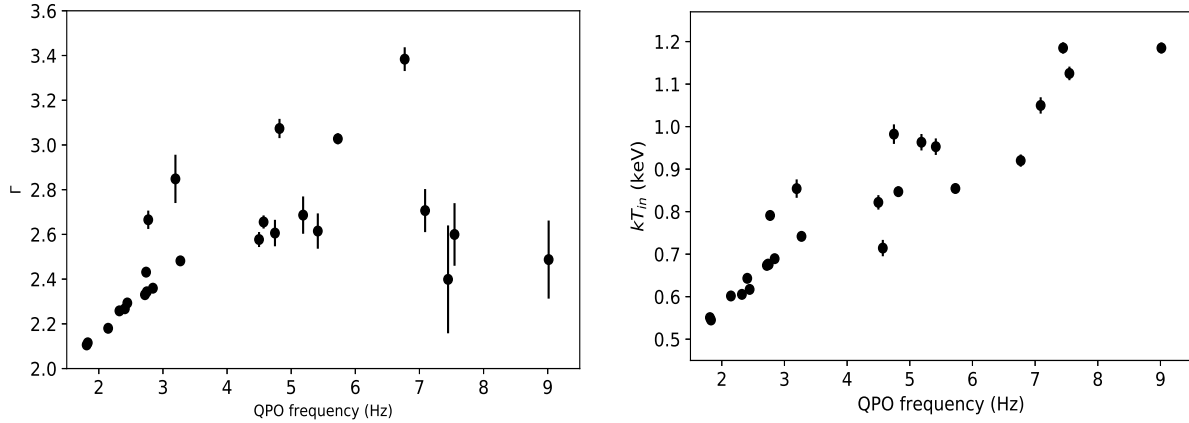


**Figure 5.** The dependence of  $\Gamma$  (left panel) and  $kT_{in}$  (right panel) upon QPO frequency in MAXI J1535–571. The values of  $\Gamma$  and  $kT_{in}$  are obtained from the fits to the time-averaged spectra, the rms and phase-lag spectra of the QPO.

quency,  $\nu_c$ .

To estimate the critical frequency, we assume that the break in the relation of the disc and corona model parameters, and time lags as a function of QPO frequency, happens at the same QPO frequency, i.e.,  $\nu_c$ . In Figure 8 we show fits with a power-law (red) and broken power-law (blue) to the relation of  $L$ ,  $kT_s$ , time lag,  $kT_{in}$  with QPO frequency. The parameters of the broken power law are the power-law indices  $\alpha_1$  and  $\alpha_2$  below and above the break frequency  $\nu_c$  and a normalisation parameter. We have calculated the F-test probability for the fits with a power law and a broken power-law and found that the probability ranges from  $(0.2 - 1) \times 10^{-4}$ , which indicates that a broken power-law in general fits the data better than a power law. (To account for the dispersion of the data points around the model was larger than the statistical errors, we have added a systematic of 6%.) The break for each individual fit is in the range 2.7–2.8 Hz, and the break appears to be at the same QPO frequency in all cases. Since there is a hint of a break in the relationship of the time lags and  $kT_{in}$  with QPO frequency, we fitted all the four relations ( $L$ ,  $kT_s$ , time lag,  $kT_{in}$ ) together with a broken power law model as shown in Figure 8, with the critical frequency tied. We got

**Table 3.** Broken power-law best-fitting parameters to the relations of  $L$ ,  $kT_s$ , time lags of the QPO and  $kT_{in}$  vs. QPO frequency shown in Figure 8. The parameters  $\alpha_1$  and  $\alpha_2$  are the power-law indices for  $\nu_{QPO} \leq \nu_c$  and  $\nu_{QPO} > \nu_c$ , respectively.

Parameter	$\alpha_1$	$\alpha_2$	bknpower norm
$L$ (km)	$1.8 \pm 0.4$	$0.5 \pm 0.2$	$(3.8 \pm 1.3) \times 10^4$
$kT_s$ (keV)	$-2.2 \pm 0.5$	$-0.3 \pm 0.2$	$0.04 \pm 0.01$
$kT_{in}$ (keV)	$-0.6 \pm 0.2$	$-0.4 \pm 0.1$	$0.7 \pm 0.1$
time lag (m sec)	$0.6 \pm 0.4$	$1.2 \pm 0.2$	$0.007 \pm 0.002$

Note: The best-fitting parameters values shown above are for the joint fits of all the parameter vs. QPO frequency plot with  $\nu_c$  tied.

$\nu_c = 3.0 \pm 0.4$  Hz. If we let  $\nu_c$  vary separately for each fit, the  $\chi^2$  changes from 141.84 (dof=88) to 133.38 (dof=85) with an F-test probability of  $\sim 0.15$ . This confirms that the best fit does not improve significantly if we let  $\nu_c$  free. We conclude that the break is consistent with being at the same frequency in all relations plotted in Figures 5 and 8. The details of the best-fitting parameters are given in Table 3.



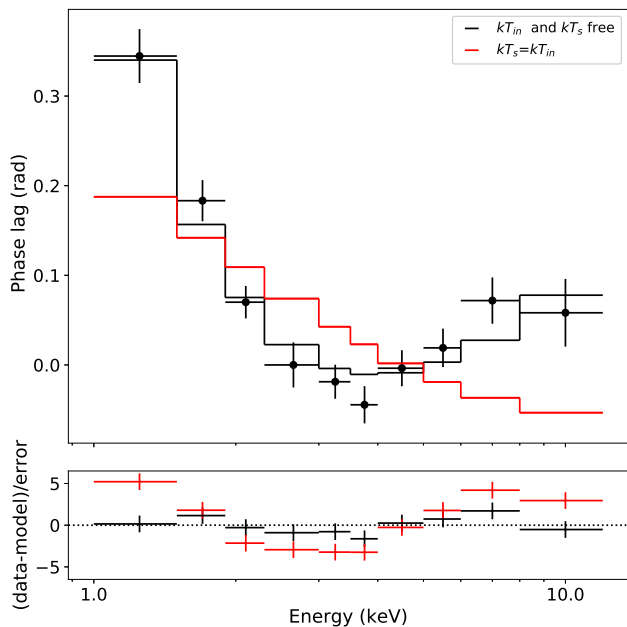


**Figure 6.** The phase-lag spectra of the QPO of MAXI J1535–571 fitted with the VKOMPTHDK model keeping  $kT_{in}$  and  $kT_s$  tied to each other (red), and free (black). The bottom panel shows the respective residuals of the fits. The data corresponds to obs ID 1050360105 with QPO frequency  $\sim 1.8$  Hz

## 4 DISCUSSION

We have analysed NICER observations of MAXI J1535–571 during the initial phase of the outburst in September and October 2017. The rms and lag spectrum of the type-C QPO, the spectral parameters deduced from fits to the time-averaged energy spectra of the source (the temperature of the accretion disc,  $kT_{in}$ ), and the parameters from fits to the rms and lag spectra of the QPO (the size of the corona,  $L$ , the temperature of the source that provides the seed photons that inverse-Compton scatter in the corona,  $kT_s$ , all change in a similar manner as the frequency of the type-C QPO increases from 1.8 Hz to 9 Hz. While some of these quantities increase ( $kT_{in}$ ,  $kT_s$ , phase lags) and others decrease (rms amplitude of the QPO,  $L$ ) with increasing QPO frequency, we find that all these quantities show a significant break in the relation at a QPO frequency  $\nu_c \sim 3.0$  Hz.

At low QPO frequencies, the lag spectrum of the type-C QPO in MAXI J1535 increases at low and high energies and is minimum at  $\sim 4$  keV. This is similar to what is observed for the type-B QPO in the black hole candidate MAXI J1348–630 (Belloni et al. 2020, García et al. 2021). In the case of MAXI J1348–630, Belloni et al. (2020) proposed that the fact that photons at energies below  $\sim 3$  keV lag behind photons at  $\sim 3$  keV is due to down scattering of the photons emitted by the disc in the corona, that they assume is the jet. To reach these conclusions, instead of a black body-like seed spectrum, Belloni et al. (2020) assumed a simplified seed-source spectrum that is flat between 2 and 3 keV and does not emit at other energies. Such a spectrum, however, neglects the dilution of the lags caused by black

body photons emitted below 2 keV that escape without being up-/down-scattered in the corona. If one considers a more realistic (a black body or a disc) seed spectrum of equivalent temperature, the lags turn out to be flat below  $\sim 2 - 3$  keV, different from what is observed (Kylafis et al. 2021). On the other hand, using the model of Karpouzas et al. (2020), García et al. (2021) showed that the shape of the lag spectrum (and the rms spectrum as well) of MAXI J1348–630 can be explained by corona photons that impinge back onto the accretion disc and emerge later and at energies below those of the photons that were up-scattered in the corona. This feedback loop between the corona and the disc is the reason for the positive lags between the photons with energies below  $\sim 2 - 3$  keV and those with energies of  $\sim 2 - 3$  keV. At the same time, inverse Compton scattering in the corona explains that photons with energies above  $\sim 2 - 3$  keV lag behind the  $2 - 3$  keV photons. Our fits to the rms and lag spectra of the QPO in MAXI J1535 here show the same.

### 4.1 Connection of critical frequency with radio jet quenching

Using ASTROSAT, and SWIFT observation of the period MJD 58008 – 58013 and 58004 – 58017, Mereminskiy et al. (2018) and Bhargava et al. (2019) found a tight correlation between the QPO frequency and the power-law index that models the hard component in the energy spectrum. Using NICER observation of the period MJD 58008.99 – 58037.68, we, on the other hand, found a significant break in the spectral and corona parameters as a function of QPO frequency. The rms and lag spectra of the QPO below and above  $\nu_c$  are also significantly different. The break in the relation between the QPO lags and QPO frequency at  $\nu_c \sim 3.0$  Hz in MAXI J1535 is similar to the break found by Zhang et al. (2020) in GRS 1915+105 when the QPO frequency is  $\sim 2$  Hz, and to the one in GX 339-4 (Zhang et al. 2017) at a QPO frequency of  $\sim 1.7$  Hz.

Interestingly, the frequency of the QPO in MAXI J1535 crosses the value of 3.0 Hz on September 17 2017 (MJD 58013; see Figure 4 and Table 1). This date coincides with the time at which the radio emission from the jet in this source is quenched (Russell et al. 2019), which we marked by the shaded area in Figure 4. Indeed, the radio emission of the jet in MAXI J1535 quenches in the period MJD 58013.60 – 58014.18; after that, in the period MJD 58014.18 – 58015.37 (Table 1 Russell et al. 2019) the source makes a transition from the hard intermediate to the soft intermediate state. A similar behaviour has been observed by Méndez et al. (2022) for GRS 1915+105, i.e., a low radio emission at or above a QPO frequency of  $\sim 2.0$  Hz, and increased radio emission below that QPO frequency, the QPO frequency at which Zhang et al. (2020) found that the lags of the QPO change from soft to hard.

### 4.2 Size of the corona

From fits to the rms and lag spectra of the QPO with the VKOMPTHDK, here we find that the size of the corona decreases very rapidly from  $\sim 10^4$  km to  $\sim 4000 - 5000$  km

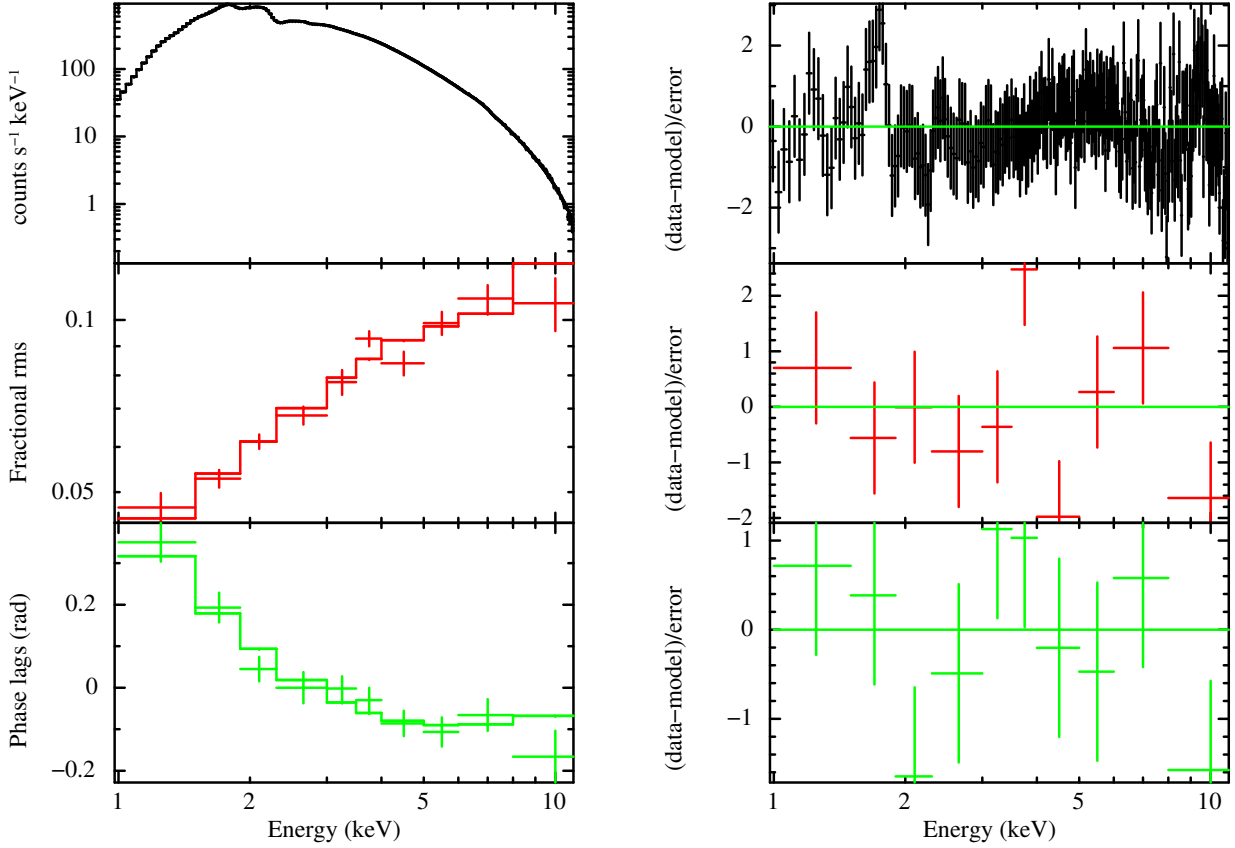


**Figure 7.** Fits of the vkompthdk model to the data of MAXI J1535—571. From top to bottom, the left panel shows the time-averaged spectrum of the source fitted with the model  $\text{TBABS}^*(\text{DISKBB}+\text{GAUSS}+\text{NTHCOMP})$ , the rms spectrum of the QPO fitted with the model  $\text{VKOMPTHDK}^*\text{DILUTION}$ , and the phase-lag spectrum of the QPO fitted with the model vkompthdk when the QPO frequency was at  $\sim 1.8$  Hz. The right panels show the respective residuals of the best-fitting model to the data. The 2.0–3.0 keV band is the reference band for the phase lag spectra.

when the QPO frequency increases from  $\sim 1.8$  Hz to  $\sim 3.2$  Hz; from that point on the corona size remains more or less constant or decreases slightly from  $\sim 4000 - 5000$  km down to  $\sim 3000$  km as the QPO frequency increases from  $\sim 3.2$  Hz up to  $\sim 9$  Hz. Figure 4 shows that the QPO frequency does not increase monotonically during these observations. In contrast, from Figures 4 and 8, it is apparent that the size of the corona first increases from  $\sim 2000$  km to  $\sim 10^4$  km, and it then decreases back to  $\sim 3000$  km (first 10 points in the right panel of Figure 4). At this time, coincident with the time that the radio emission from the jet is quenched (Russell et al. 2019), the size of the corona continues decreasing but at a lower rate than before. Assuming that MAXI J1535 harbours a 10-solar mass black hole, the maximum and minimum size of the corona are, respectively,  $\sim 670$  and  $\sim 201 R_g$ .

At low QPO frequency, the trends of the corona size and feedback fraction as a function of QPO frequency reported

in this work are similar to those in Zhang et al. (2022), and both in their work and ours the relation between the size of the corona and the frequency of the QPO shows a break at  $\nu_{\text{QPO}} \approx 3 - 4$  Hz. The difference between their and our corona sizes in the common range of QPO frequency comes from the coverage down to lower energies with NICER in our case than in Zhang et al. (2022) with HXMT: The magnitude of the lags of the QPO increases as energy decreases, and the size of the corona in the vkompth model is driven by the magnitude of the lags. Since we go to lower QPO frequencies than Zhang et al. (2022), we find that the size of the corona continues increasing as the QPO frequency decreases below  $\sim 2$  Hz, where they do not have data. At QPO frequencies above  $\sim 4$  Hz Zhang et al. (2022) find an increase of the corona size, whereas here we find that the size continues decreasing with QPO frequency, albeit at a slower rate than below  $\sim 3 - 4$  Hz. We note that Zhang et al. (2022) did not include the effect of dilution of the non-variable components

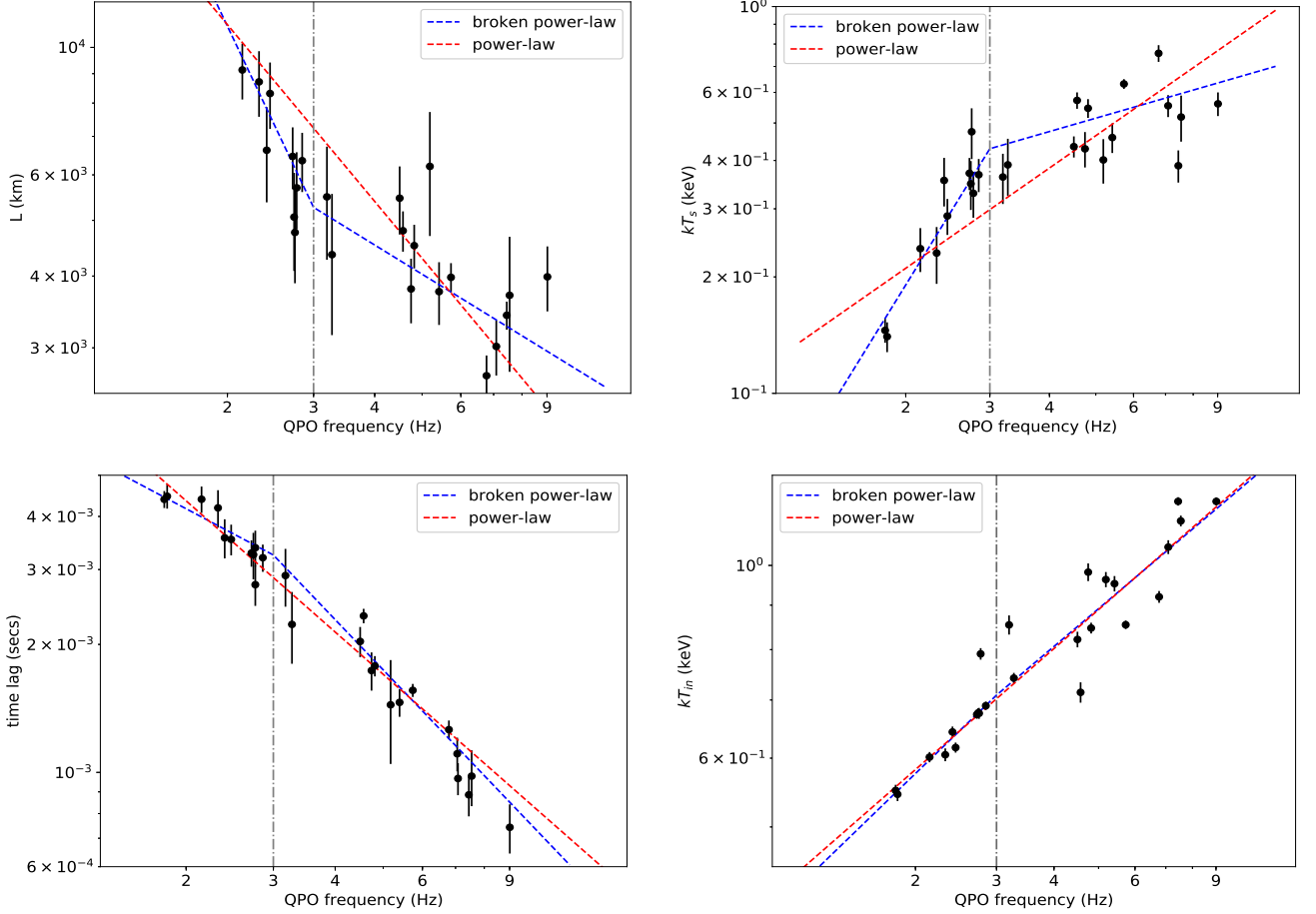


**Figure 8.** Dependence of  $L$ ,  $kT_s$ , time lags of the QPO and  $kT_{in}$  upon QPO frequency in MAXI J1535 –571. The red and blue dotted lines show the best-fitting power law and a broken power-law to the data. The best-fitting parameters for each relation are given in Table 3. The time lags are between photons in the 1.0–12.0 keV and 2.0–6.0 keV bands at the QPO frequency. The vertical dotted dashed line represents the best-fitting break frequency,  $\nu_c = 3.0$  Hz.

the rms amplitude of the QPO in their model, and that dilution is more important at high QPO frequency, where the contribution of the accretion disc to the total emission increases.

Our result is similar to previous findings in other BHXBs (e.g. Kara et al. 2019, Karpouzas et al. 2021). In contrast to Kara et al. (2019) where a change of the vertical size of the corona is proposed to explain the shorter reverberation lags for MAXI J1820+070, De Marco et al. (2021) infer a change in the inner accretion disc radius leading to smaller coronal size than reported in this work. Using the JED-SAD model for the same source, Marino et al. (2021) reported that the size of the jet emitting region, which plays the corona role in their model, of  $30\text{--}60 R_g$ . Axelsson & Veledina (2021) showed that the variability of the iron line feature could not be explained using the lamp-post geometry assumed by Kara et al. (2019) and, instead, a truncated inner hot flow geometry is required. Using a spectral-timing model based on propagating fluctuations and incorporating the reverberation from the variable Comptonisation components, Kawamura et al. (2022) further supported a truncated inner hot flow geometry. However, we note that the mass accretion

rate propagation fluctuation mechanism used by Kawamura et al. (2022) can only explain the hard lags, and a separate mechanism is required to explain the soft lags in MAXI J1820+070 and in the QPO of MAXI J1535–571 and other sources.

The trend of the size of the corona vs QPO frequency is similar in MAXI J1535–571 and GRS 1915+105 (see Figure 8, and the supplementary Figure 4 in Méndez et al. 2022 and figure 5 in García et al. 2022). Using a reverberation model for the lags of the broadband noise component in the power spectrum, Wang et al. (2021) found a corona that is  $\gtrsim 300 R_g$  in the hard to soft state transition of MAXI J1820+070. Similarly, using polarimetry measurements with PoGO+, Chauvin et al. (2018) found that the corona in Cyg X-1 is  $\gtrsim 100 R_g$ , while they exclude a corona of  $\sim 6 R_g$  obtained from the lamp post model. The sizes reported in this work are consistent with the values published by Kylafis & Reig (2019), Kylafis et al. (2021), Reig & Kylafis (2021), who used Monte Carlo simulations of Comptonization in a jet. The Comptonization model used in this work has some simplifications; for instance, the corona is spherically symmetric with constant temperature and optical depth.

This was discussed in Karpouzas et al. (2021), and García et al. (2021) and, as explained in Méndez et al. (2022), since the actual geometry of the corona is likely different, the values given by the model should be considered as a characteristic size of the corona rather than the actual radius of a spherical corona (see Méndez et al. 2022; García et al. 2022).

The size of the corona that we infer from our model is larger than the values obtained from fits to the energy spectra of black-hole systems with models that consider reflection off the accretion disc from a corona that is assumed to be a lamppost emitter (e.g., Vincent et al. 2016). These spectral fits yield corona sizes of  $1 - 20 R_g$  (Fabian et al. 2012). Using the average soft lags over a broad frequency range in the power spectrum and light travel-time arguments, Wang et al. (2022) found that corona sizes in a dozen black-hole systems in the hard-intermediate state, during the transition from the low-hard to the soft-intermediate state, are comparable, within a factor of a few, to the ones we infer here (see also Wang et al. 2021). Suppose the assumption that the lags of the broadband noise reflect the light travel time from the corona to the disc is correct. In that case, the corona sizes in Wang et al. (2022) are, in fact, lower limits for two reasons: (i) Wang et al. (2022) estimate the corona sizes based on the average time lag over a broad frequency range, whereas the magnitudes of the soft lags are larger than the average over a large range of QPO frequencies (see, for instance, their Fig. 3, panel h). (ii) Wang et al. (2022) measured the lags between the bands  $0.5 - 1$  and  $2 - 5$  keV. Suppose the lags are minimum at around  $\sim 2$  keV and increase both at energies below and above that (see their Fig. 3, panel g). In that case, the magnitude of the time lags between photons at  $\sim 2$  and  $\sim 0.5$  keV, and hence the light travel distance from the corona to the disc will be larger than what they report. Notice, however, that in Kara et al. 2019, Wang et al. 2021 and Wang et al. 2022, the authors estimate the characteristic height of the lamppost corona above the disc.

Notice that it is not straightforward to infer sizes from simple light travel-time arguments applied to the time lags of the broadband noise components because: (i) The broadband noise component in the power spectrum of accreting black-hole and neutron-star systems is, in fact, the combination of multiple Lorentzians (e.g., Psaltis et al. 1999, Nowak 2000). Since the properties of these Lorentzians are correlated with each other (e.g., frequency-frequency correlations in Psaltis et al. 1999) and with the source spectral parameters (e.g., Vignarca et al. 2003; Mereminskiy et al. 2018; Agrawal 2006 and references therein), therefore, most likely, these Lorentzians are not just an empirical description of the power spectrum, but each of them represents a relatively well-defined, over a limited frequency range, variability component of the physical properties of the accretion flow. Suppose this decomposition is correct (as suggested by the works cited above). In that case, a more logical and accurate way is to compute the phase lag that results from the combined cross spectra of these Lorentzians in the Fourier real and imaginary space. The phase-lag calculated like that can be different from computed from the average of the cross-spectrum over a broad frequency range (as has been done in many works before, see, e.g. Nowak et al. 1999a; Reig et al. 2000; Altamirano & Méndez 2015;

Wang et al. 2022). If the lags calculated from the Lorentzian decomposition, as suggested above, were due to light travel time, the magnitude of time lags (see, for instance, Fig. 6) imply large corona sizes. So even combining the lags of the Lorentzians in Fourier space will lead to big corona sizes. ii) It needs to be clarified how to convert time lags into distances using simple light travel-time arguments because the lags depend strongly upon Fourier frequency (e.g., Fig. 3 panel h of Wang et al. 2022). Therefore, there is no single Fourier frequency at which the time lag would represent the correct light travel time that should be used to infer the corona size. (We note that models like RELTRANS, Ingram et al. (2019) calculate the full variability self consistently instead of using simple light travel-time arguments.) Given the typical magnitudes of the lags of the QPO (this paper; Karpouzas et al. 2020; García et al. 2021; Karpouzas et al. 2021; Bellavita et al. 2022) or of the broadband noise component (Wang et al. 2022; but see above for the caveats of these measurements) in these systems, any variability model that interprets the observed lags as delays of photons travelling through a medium around a compact object would necessarily yield large corona sizes since time lags of a few hundredths to a few tenths of seconds translate into light travel distances of a few thousand to a few 10,000 km. While propagation of accretion-rate fluctuations (Arévalo & Uttley 2006) would yield smaller sizes of the comptonizing region because, in this case, the viscous time scale is at play, propagation of accretion-rate fluctuations only account for hard lags. In contrast, the broadband noise component and the QPOs often show soft lags.

Our results are not necessarily inconsistent with the QPO frequency being due to Lense-Thirring Precession (LTP, Stella & Vietri 1998; but see Mastichiadis et al. 2022). For instance, Ingram et al. (2016) fitted the energy spectra of the BHXRB H1743–322 over the cycle of a  $\sim 4-5$  QPO and concluded that the results are consistent with LTP of an inner hot torus in this source. However, as explained by Ingram et al. (2016), their data could be reproduced equally well if the torus was fixed and it was the disc the one that processed at the Lense-Thirring precession frequency. Their choice of one geometry over the other was based on the fact that the rms spectrum of the QPO is hard, and hence the emission at the QPO frequency could not come from the disc. In the model of Karpouzas et al. (2020), the rms spectrum of the QPO is a consequence of inverse-Compton scattering of soft disc photons in the corona (the torus in the scenario of Ingram et al. 2016), such that the high rms amplitude values of the QPO at high energies may reflect the variability of the soft disc emission at the Lense-Thirring precession frequency that is inverse-Compton scattered in the corona. This, plus the feedback from the corona to the disc, naturally explain the variability of the iron line discussed by Ingram et al. (2016) and the rms spectrum of the QPO. The LTP model and the reverberation model for the lags of the QPO in GRS 1915+105 (Nathan et al. 2022) also yield a large corona (unless one considers an extra lag due to thermalisation; see Nathan et al. 2022). Therefore, the LTP model needs to explain how a large corona, which should necessarily extend beyond the disc's inner truncation radius, can precess as a solid body. However, whether the QPO frequency is due to LTP is a matter of debate that needs to be addressed

by general relativistic magneto-hydrodynamic (GRMHD) simulations, which is beyond the scope of this paper.

### 4.3 A Dual Corona

When we tied the inner-disc temperature of the time-averaged spectra,  $kT_{in}$ , to the seed-photon temperature of the VKOMPTHDK model,  $kT_s$ , our fits could not reproduce the shape of the lag spectrum. Letting these two parameters free yields a significant improvement in the fit statistics (see Section 3.3 and Figure 6). We speculate that this difference between the seed photon temperature of NTHCOMP and VKOMPTHDK is due to a more complex structure of the comptonizing region than that described by a uniform corona. Sridhar et al. (2019), Bhargava et al. (2019) & Garg et al. (2022) used AstroSat observations of MAXI J1535 that coincide with the first few days of the NICER observations reported in this work. They modelled the combined SXT and LAXPC spectra and reported a lower inner disc temperature ( $kT_{in}=0.20\text{--}0.35$  keV) than we found in this work. It should be noted that Bhargava et al. (2019) and Garg et al. (2022) modelled the spectra in the 1–30 keV energy range. Also, the source is highly absorbed, and the spectrum drops at low energies, so the reported inner disc temperature may not be accurate. Sreehari et al. (2019) used the same AstroSat observation and modelled the broadband spectra in the 0.3–80.0 keV band and reported electron temperatures with NTHCOMP in the range 21–63 keV. Using the same AstroSat observation, Sridhar et al. (2019) reported an electron temperature of  $\sim 21$  keV. As the 0.8–10.0 keV spectra of NICER could not constrain the electron temperature, we chose to fix it to the values reported by Sreehari et al. (2019) and Sridhar et al. (2019). The electron temperature ( $\sim 90\text{--}108$  keV) reported by Garg et al. 2022 is higher than the value ( $\sim 21$  keV) we have used in this work. It should be noted that in Garg et al. (2022), they are fixed the optical depth of the corona, which together with  $\Gamma$  gives  $kT_e$ .

Using a dual-component comptonization model for type-B QPOs, García et al. (2021) and Peirano et al. (2022) argued that the comptonizing medium of the BHXB sources, MAXI J1348–630 and GX 339–4 consist of two coronas. A relatively small corona of  $\sim 300$  km, close to the black hole dominates the time-averaged spectra, and a large corona of  $\sim 18000$  km, possibly the jet, dominates the lag spectrum (Peirano et al. 2022). Their best-fitting results yield a lower seed photon temperature of the large corona compared to the small corona, with the seed photon temperature of the small corona linked to  $kT_{bb}$  of NTHCOMP. Peirano et al. (2022) proposed that this difference is due to the fact that the seed photons for the small corona come from the inner, hotter parts, of the disc whereas the seed photons for the large corona come from the outer, cooler parts, of the disc. A similar dual-corona geometry could explain the difference between  $kT_{in}$  of the DISKBB (linked to  $kT_{bb}$  of NTHCOMP) and  $kT_s$  of VKOMPTHDK in our fits. Since we find that  $kT_{bb} > kT_s$ , also in MAX J1535–571 the small corona would dominate the emission of the time-averaged spectra, whereas the big corona would dominate the lags. We found that the rms spectra do not change much between the two fits ( $kT_s=kT_{in}$  or  $kT_s$  free), so we conclude that the rms amplitude is not affected much

by the size of the corona. The fraction of the corona flux that returns to the disc is  $\eta_{int}$  10–25 % in all the cases. This and the large corona size further indicate that the large corona is the jet.

## 5 SUMMARY AND CONCLUSIONS

We have analysed all NICER observation of MAXI J1535–571 taken on September and October 2017. We fit the energy spectra of the source and the rms and lag spectra of the type-C QPO in this source with the one-component time dependent Comptonization model VKOMPTHDK. Below we summarize our results:

- The size of the corona of MAXI J1535–571 decreases from  $10^4$  km when the QPO frequency is  $\geq 2$  Hz to  $\sim 3000$  km when the QPO frequency is  $\sim 9.0$  Hz.
- The behaviour of all the spectral parameters and the rms and lag spectra of the QPO changes above and below a critical QPO frequency,  $\nu_c = 3.0 \pm 0.4$  Hz. Interestingly, the time at which this critical frequency happens coincide with the period when the radio jet emission quenches for this source.
- Comparing our results with those in previous work, the data are consistent with a dual corona: a small corona lying close to the black hole and a larger one, possibly the jet.

## ACKNOWLEDGEMENTS

This research is part of a project proposed for the COSPAR PCB fellowship program. We would like to thank the referee for constructive comments that helped improve this paper. DR would like to thank COSPAR, ISRO and Professor Diego Altamirano for jointly funding the academic visit to the University of Southampton. MM, FG and KK acknowledge support from the research programme Athena with project number 184.034.002, which is (partly) financed by the Dutch Research Council (NWO). FG acknowledges support from PIP 0102 and PIP 0113 (CONICET). FG is a CONICET researcher. This work received financial support from PICT-2017-2865 (ANPCyT). KA acknowledges support from a UGC-UKIERI Phase 3 Thematic Partnership (UGC-UKIERI-2017-18-006; PI: P. Gandhi). TMB acknowledges financial contribution from PRIN INAF 2019 n.15. CB is a fellow of Consejo Interuniversitario Nacional (CIN).

## DATA AVAILABILITY

The NICER XTI observations used in this work are available at NICER Archive<sup>6</sup>.

## REFERENCES

- Agrawal P. C., 2006, *Advances in Space Research*, 38, 2989  
 Altamirano D., Méndez M., 2015, *MNRAS*, 449, 4027  
 Altamirano D., Strohmayer T., 2012, *ApJ*, 754, L23  
 Arévalo P., Uttley P., 2006, *MNRAS*, 367, 801

<sup>6</sup> [https://heasarc.gsfc.nasa.gov/docs/nicer/nicer\\_archive.html](https://heasarc.gsfc.nasa.gov/docs/nicer/nicer_archive.html)



- Axelsson M., Veledina A., 2021, *MNRAS*, **507**, 2744
- Bellavita C., García F., Méndez M., Karpouzas K., 2022, *MNRAS*, **515**, 2099
- Belloni T., Hasinger G., 1990, *A&A*, **230**, 103
- Belloni T. M., Stella L., 2014, *Space Sci. Rev.*, **183**, 43
- Belloni T., Psaltis D., van der Klis M., 2002, *ApJ*, **572**, 392
- Belloni T., Homan J., Casella P., van der Klis M., Nespoli E., Lewin W. H. G., Miller J. M., Méndez M., 2005, *A&A*, **440**, 207
- Belloni T. M., Motta S. E., Muñoz-Darias T., 2011, Bulletin of the Astronomical Society of India, **39**, 409
- Belloni T. M., Sanna A., Méndez M., 2012, *MNRAS*, **426**, 1701
- Belloni T. M., Zhang L., Kylafis N. D., Reig P., Altamirano D., 2020, *MNRAS*, **496**, 4366
- Bhargava Y., Belloni T., Bhattacharya D., Misra R., 2019, *MNRAS*, **488**, 720
- Casella P., Belloni T., Homan J., Stella L., 2004, *A&A*, **426**, 587
- Casella P., Belloni T., Stella L., 2005, *ApJ*, **629**, 403
- Chauhan J., et al., 2019, *MNRAS*, **488**, L129
- Chauvin M., et al., 2018, *Nature Astronomy*, **2**, 652
- Chen X., Swank J. H., Taam R. E., 1997, *ApJ*, **477**, L41
- Cúneo V. A., et al., 2020, *MNRAS*, **496**, 1001
- De Marco B., Zdziarski A. A., Ponti G., Migliori G., Belloni T. M., Segovia Otero A., Dzielak M. A., Lai E. V., 2021, *A&A*, **654**, A14
- Dewangan G. C., Titarchuk L., Griffiths R. E., 2006, *ApJ*, **637**, L21
- Diğer T., 2017, The Astronomer's Telegram, **10716**, 1
- Done C., Gierliński M., Kubota A., 2007, *A&A Rev.*, **15**, 1
- Fabian A. C., et al., 2012, *MNRAS*, **424**, 217
- Fender R. P., Belloni T. M., Gallo E., 2004, *MNRAS*, **355**, 1105
- García F., Méndez M., Karpouzas K., Belloni T., Zhang L., Altamirano D., 2021, *MNRAS*, **501**, 3173
- García F., Karpouzas K., Méndez M., Zhang L., Zhang Y., Belloni T., Altamirano D., 2022, *MNRAS*, **513**, 4196
- Garg A., Misra R., Sen S., 2022, *MNRAS*, **514**, 3285
- Gendreau K. C., Arzoumanian Z., Okajima T., 2012, in Takahashi T., Murray S. S., den Herder J.-W. A., eds, Society of Photo-Optical Instrumentation Engineers (SPIE) Conference Series Vol. 8443, Space Telescopes and Instrumentation 2012: Ultraviolet to Gamma Ray. p. 844313, doi:10.1117/12.926396
- Gendreau K. C., et al., 2016, in den Herder J.-W. A., Takahashi T., Bautz M., eds, Society of Photo-Optical Instrumentation Engineers (SPIE) Conference Series Vol. 9905, Space Telescopes and Instrumentation 2016: Ultraviolet to Gamma Ray. p. 99051H, doi:10.1117/12.2231304
- Gendreau K., et al., 2017, The Astronomer's Telegram, **10768**, 1
- Gilfanov M., 2010, in Belloni T., ed., , Vol. 794, Lecture Notes in Physics, Berlin Springer Verlag. Springer Berlin Heidelberg, p. 17, doi:10.1007/978-3-540-76937-8\_2
- Homan J., Wijnands R., van der Klis M., Belloni T., van Paradijs J., Klein-Wolt M., Fender R., Méndez M., 2001, *ApJS*, **132**, 377
- Huang Y., et al., 2018, *ApJ*, **866**, 122
- Ingram A. R., Motta S. E., 2019, *New A Rev.*, **85**, 101524
- Ingram A., van der Klis M., Middleton M., Done C., Altamirano D., Heil L., Uttley P., Axelsson M., 2016, *MNRAS*, **461**, 1967
- Kara E., et al., 2019, *Nature*, **565**, 198
- Karpouzas K., Méndez M., Ribeiro E. M., Altamirano D., Blaes O., García F., 2020, *MNRAS*, **492**, 1399
- Karpouzas K., Méndez M., García F., Zhang L., Altamirano D., Belloni T., Zhang Y., 2021, *MNRAS*, **503**, 5522
- Kawamura T., Done C., Axelsson M., Takahashi T., 2022, arXiv e-prints, p. arXiv:2209.14492
- Kennea J. A., Evans P. A., Beardmore A. P., Krimm H. A., Romano P., Yamaoka K., Serino M., Negoro H., 2017, The Astronomer's Telegram, **10700**, 1
- Koljonen K. I. I., Hannikainen D. C., McCollough M. L., 2011, *MNRAS*, **416**, L84
- Kumar N., Misra R., 2014, *MNRAS*, **445**, 2818
- Kylafis N. D., Reig P., 2019, in High Energy Phenomena in Relativistic Outflows VII. p. 37 (arXiv:1911.11975)
- Kylafis N. D., Trümper J. E., Loudas N. A., 2021, *A&A*, **655**, A39
- Ma X., et al., 2021, *Nature Astronomy*, **5**, 94
- Makishima K., Maejima Y., Mitsuda K., Bradt H. V., Remillard R. A., Tuohy I. R., Hoshi R., Nakagawa M., 1986, *ApJ*, **308**, 635
- Marino A., et al., 2021, *A&A*, **656**, A63
- Markwardt C. B., Burrows D. N., Cummings J. R., Kennea J. A., Marshall F. E., Page K. L., Palmer D. M., Siegel M. H., 2017, GRB Coordinates Network, **21788**, 1
- Mastichiadis A., Petropoulou M., Kylafis N. D., 2022, *A&A*, **662**, A118
- Méndez M., van der Klis M., 1997, *ApJ*, **479**, 926
- Méndez M., Altamirano D., Belloni T., Sanna A., 2013, *MNRAS*, **435**, 2132
- Méndez M., Karpouzas K., García F., Zhang L., Zhang Y., Belloni T. M., Altamirano D., 2022, *Nature Astronomy*, **6**, 577
- Mereminskiy I. A., Grebenev S. A., Prosvetov A. V., Semena A. N., 2018, *Astronomy Letters*, **44**, 378
- Miller J. M., et al., 2001, *ApJ*, **563**, 928
- Miller J. M., et al., 2018, *ApJ*, **860**, L28
- Mitsuda K., et al., 1984, *PASJ*, **36**, 741
- Motta S. E., Casella P., Henze M., Muñoz-Darias T., Sanna A., Fender R., Belloni T., 2015, *MNRAS*, **447**, 2059
- Nakahira S., et al., 2018, *PASJ*, **70**, 95
- Nathan E., et al., 2022, *MNRAS*, **511**, 255
- Negoro H., et al., 2017a, The Astronomer's Telegram, **10699**, 1
- Negoro H., et al., 2017b, The Astronomer's Telegram, **10708**, 1
- Nowak M. A., 2000, *MNRAS*, **318**, 361
- Nowak M. A., Dove J. B., Vaughan B. A., Wilms J., Begelman M. C., 1999a, *Nuclear Physics B Proceedings Supplements*, **69**, 302
- Nowak M. A., Vaughan B. A., Wilms J., Dove J. B., Begelman M. C., 1999b, *ApJ*, **510**, 874
- Parikh A. S., Russell T. D., Wijnands R., Miller-Jones J. C. A., Sivakoff G. R., Tetarenko A. J., 2019, *ApJ*, **878**, L28
- Pasham D. R., Strohmayer T. E., Mushotzky R. F., 2013, *ApJ*, **771**, L44
- Peirano V., Méndez M., García F., Belloni T., 2022, arXiv e-prints, p. arXiv:2212.00062
- Psaltis D., Belloni T., van der Klis M., 1999, *ApJ*, **520**, 262
- Rawat D., et al., 2019, *ApJ*, **870**, 4
- Reig P., Kylafis N. D., 2021, *A&A*, **646**, A112
- Reig P., Belloni T., van der Klis M., Méndez M., Kylafis N. D., Ford E. C., 2000, *ApJ*, **541**, 883
- Remillard R. A., McClintock J. E., 2006, *ARA&A*, **44**, 49
- Remillard R. A., Sobczak G. J., Munro M. P., McClintock J. E., 2002, *ApJ*, **564**, 962
- Russell T. D., Miller-Jones J. C. A., Sivakoff G. R., Tetarenko A. J., Japote Xrb Collaboration 2017, The Astronomer's Telegram, **10711**, 1
- Russell T. D., et al., 2019, *ApJ*, **883**, 198
- Scaringi S., ASTR211 Students 2017, The Astronomer's Telegram, **10702**, 1
- Sreehari H., Ravishankar B. T., Iyer N., Agrawal V. K., Katoh T. B., Mandal S., Nandi A., 2019, *MNRAS*, **487**, 928
- Sridhar N., Bhattacharyya S., Chandra S., Antia H. M., 2019, *MNRAS*, **487**, 4221
- Stella L., Vietri M., 1998, *ApJ*, **492**, L59
- Stevens A. L., et al., 2018, *ApJ*, **865**, L15
- Stiele H., Kong A. K. H., 2018, *ApJ*, **868**, 71
- Strohmayer T. E., 2001, *ApJ*, **552**, L49
- Takizawa M., et al., 1997, *ApJ*, **489**, 272
- Tao L., et al., 2018, *MNRAS*, **480**, 4443

- Verner D. A., Ferland G. J., Korista K. T., Yakovlev D. G., 1996, [ApJ](#), **465**, 487
- Vignarca F., Migliari S., Belloni T., Psaltis D., van der Klis M., 2003, [A&A](#), **397**, 729
- Vincent F. H., Różańska A., Zdziarski A. A., Madej J., 2016, [A&A](#), **590**, A132
- Wang J., et al., 2021, [ApJ](#), **910**, L3
- Wang J., et al., 2022, [ApJ](#), **930**, 18
- Wijnands R., Homan J., van der Klis M., 1999, [ApJ](#), **526**, L33
- Wilms J., Allen A., McCray R., 2000, [ApJ](#), **542**, 914
- Xu Y., et al., 2018, [ApJ](#), **852**, L34
- Zdziarski A. A., Johnson W. N., Magdziarz P., 1996, [MNRAS](#), **283**, 193
- Zhang L., Wang Y., Méndez M., Chen L., Qu J., Altamirano D., Belloni T., 2017, [ApJ](#), **845**, 143
- Zhang L., et al., 2020, [MNRAS](#), **494**, 1375
- Zhang Y., et al., 2022, [MNRAS](#), **512**, 2686
- Życki P. T., Done C., Smith D. A., 1999, [MNRAS](#), **309**, 561
- van der Klis M., Jansen F. A., 1985, [Nature](#), **313**, 768

## APPENDIX A:

**Table A.1.** The columns are the observation number, the chi-square of the fit to the steady-state spectrum ( $\chi^2_{SSS}$ ), rms spectrum ( $\chi^2_{rms}$ ), lag spectrum ( $\chi^2_{lag}$ ) with, in each case, the number of channels in each spectrum and the total reduced chi-square of the combined fit with degree of freedom.

Obs no.	$\chi^2_{SSS}$ (channel)	$\chi^2_{rms}$ (channel)	$\chi^2_{lag}$ (channel)	$\chi^2_{total}$ (dof)
1	206.9 (238)	15.5 (10)	9.0 (10)	231.4 (243)
2	176.5 (237)	7.8 (10)	7.6 (10)	191.9 (242)
3	219.5 (238)	7.7 (10)	13.3 (10)	240.5 (243)
4	205.6 (238)	4.7 (10)	9.4 (10)	219.8 (243)
5	206.8 (238)	13.8 (10)	21.8 (10)	242.3 (243)
6	167.9 (238)	5.1 (10)	4.8 (10)	177.9 (243)
7	165.9 (238)	5.0 (10)	2.4 (10)	173.2 (243)
8	227.7 (238)	4.8 (10)	2.3 (10)	234.8 (243)
9	157.1 (238)	5.0 (10)	7.2 (10)	169.3 (243)
10	146.1 (238)	4.7 (10)	4.3 (10)	155.1 (243)
11	176.4 (217)	13.0 (10)	2.7 (10)	192.2 (222)
12	129.3 (238)	10.6 (10)	12.5 (10)	152.4 (243)
13	157.3 (238)	7.3 (10)	11.8 (10)	176.3 (243)
14	147.0 (238)	17.7 (10)	3.8 (10)	168.4 (242)
15	183.9 (235)	9.3 (10)	2.7 (10)	195.8 (239)
16	146.9 (238)	13.3 (7)	4.8 (7)	165.0 (236)
17	142.4 (238)	23.0 (10)	11.6 (10)	177.0 (242)
18	240.5 (231)	3.0 (7)	0.9 (7)	244.4 (229)
19	184.0 (238)	10.5 (10)	9.1 (10)	203.6 (242)
20	185.3 (235)	3.7 (10)	15.5 (10)	204.5 (240)
21	181.6 (216)	11.6 (7)	5.1 (7)	198.2 (215)
22	211.3 (214)	23.1 (10)	23.6 (10)	258.0 (219)
23	183.8 (232)	26.2 (10)	13.1 (11)	223.1 (238)
24	184.1 (238)	5.0 (10)	2.3 (9)	191.4 (241)
25	159.6 (238)	5.2 (10)	10.1 (10)	174.9 (242)

Note: Notice that some parameters are linked in the combined fits and therefore we cannot give the number of degrees of freedom for each individual fit. So, channel numbers for individual spectra are given here.

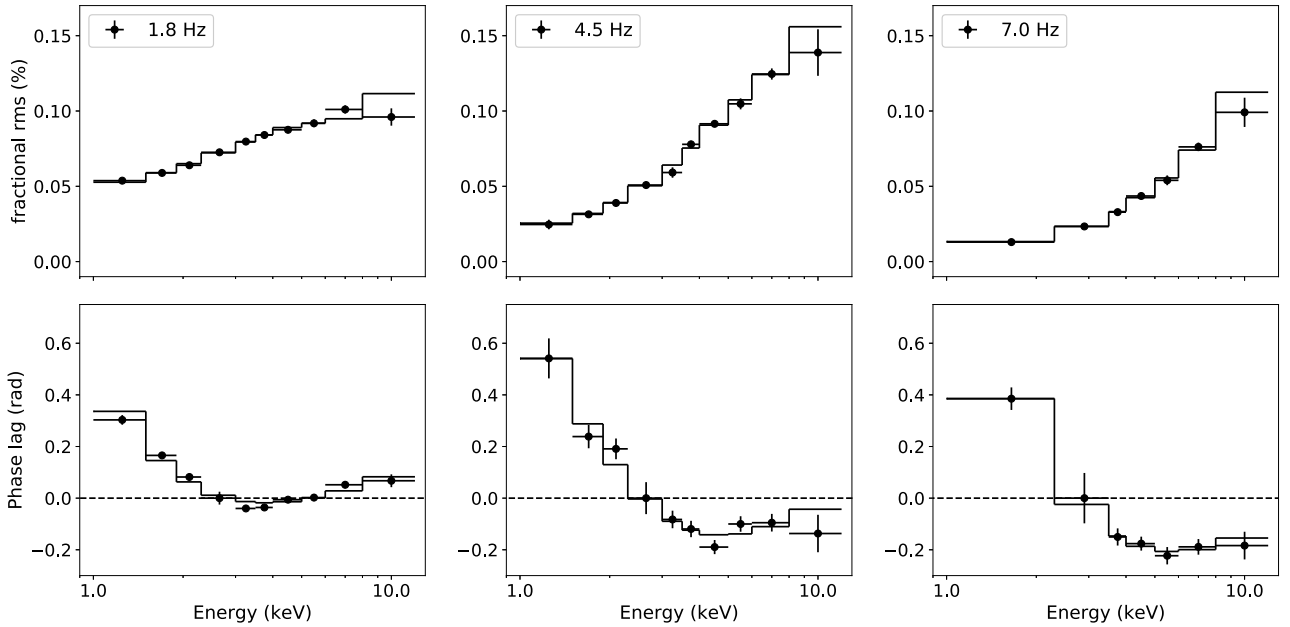


**Figure A1.** The top and bottom panels show respectively the fractional rms and phase-lag spectra of the type-C QPO in MAXI J1535–571 fitted with VKOMPTHDK model. The 2.0–3.0 keV band is the reference band for the phase lag spectra.

**Table A.2.** The columns are the observation number, QPO frequency, QPO fractional rms amplitude and time lags at the QPO frequency of MAXI J1535–571. Here rms1 and lag1 are in the 0.5–2.0 keV band, rms2 and lag2 are in the 2.0–4.0 keV band, and rms3 and lag3 are in the 4.0–10.0 keV band. The reference band for lags is 0.5–10.0 keV.

Obs no.	QPO frequency (Hz)	QPO fractional rms1 (%)	lag1 (msec)	QPO fractional rms2 (%)	lag2 (msec)	QPO fractional rms3 (%)	lag3 (msec)
1	$2.74 \pm 0.01$	$5.2 \pm 0.1$	$10.2 \pm 1.0$	$7.3 \pm 0.2$	$-1.49 \pm 0.38$	$9.4 \pm 0.3$	$-6.4 \pm 0.7$
2	$2.44 \pm 0.01$	$5.0 \pm 0.2$	$12.5 \pm 0.9$	$6.7 \pm 0.2$	$-2.22 \pm 0.41$	$8.7 \pm 0.3$	$-7.1 \pm 0.7$
3	$2.32 \pm 0.01$	$5.5 \pm 0.2$	$12.7 \pm 1.2$	$6.8 \pm 0.3$	$-3.20 \pm 0.54$	$8.8 \pm 0.4$	$-6.0 \pm 1.1$
4	$1.83 \pm 0.01$	$5.8 \pm 0.1$	$12.5 \pm 0.8$	$7.4 \pm 0.2$	$-4.63 \pm 0.38$	$8.7 \pm 0.3$	$-2.7 \pm 0.7$
5	$1.81 \pm 0.00$	$5.8 \pm 0.1$	$12.1 \pm 0.5$	$7.4 \pm 0.1$	$-4.20 \pm 0.22$	$9.2 \pm 0.1$	$-3.2 \pm 0.4$
6	$2.15 \pm 0.01$	$5.6 \pm 0.2$	$14.0 \pm 0.9$	$7.1 \pm 0.2$	$-3.24 \pm 0.39$	$8.6 \pm 0.3$	$-7.1 \pm 0.7$
7	$2.41 \pm 0.01$	$5.8 \pm 0.2$	$13.3 \pm 1.2$	$7.7 \pm 0.3$	$-1.59 \pm 0.47$	$9.8 \pm 0.4$	$-9.4 \pm 0.9$
8	$2.77 \pm 0.01$	$5.5 \pm 0.2$	$12.6 \pm 1.1$	$7.6 \pm 0.2$	$-2.05 \pm 0.42$	$9.5 \pm 0.4$	$-6.9 \pm 0.9$
9	$2.75 \pm 0.02$	$5.3 \pm 0.2$	$12.3 \pm 1.3$	$7.2 \pm 0.2$	$-1.35 \pm 0.57$	$10.0 \pm 0.4$	$-8.4 \pm 1.1$
10	$3.27 \pm 0.02$	$4.9 \pm 0.2$	$9.1 \pm 1.5$	$7.1 \pm 0.3$	$-1.44 \pm 0.54$	$10.6 \pm 0.4$	$-5.5 \pm 1.0$
11	$3.19 \pm 0.03$	$5.3 \pm 0.3$	$12.6 \pm 1.7$	$7.0 \pm 0.3$	$-1.42 \pm 0.65$	$10.5 \pm 0.5$	$-7.1 \pm 1.1$
12	$2.72 \pm 0.01$	$4.7 \pm 0.2$	$13.7 \pm 0.9$	$6.9 \pm 0.2$	$-1.79 \pm 0.33$	$9.3 \pm 0.3$	$-8.1 \pm 0.6$
13	$2.84 \pm 0.01$	$5.4 \pm 0.2$	$13.1 \pm 0.9$	$7.6 \pm 0.2$	$-2.10 \pm 0.32$	$10.4 \pm 0.3$	$-6.7 \pm 0.6$
14	$4.75 \pm 0.01$	$3.2 \pm 0.3$	$9.3 \pm 0.8$	$5.6 \pm 0.1$	$0.23 \pm 0.24$	$9.7 \pm 0.2$	$-6.2 \pm 0.4$
15	$9.01 \pm 0.04$	—	$4.4 \pm 0.4$	$1.5 \pm 0.1$	$0.07 \pm 0.15$	$3.7 \pm 0.1$	$-3.2 \pm 0.2$
16	$7.54 \pm 0.05$	$1.4 \pm 0.4$	$6.4 \pm 0.6$	$2.2 \pm 0.3$	$0.50 \pm 0.26$	$6.0 \pm 0.2$	$-4.7 \pm 0.3$
17	$7.54 \pm 0.06$	$1.3 \pm 0.2$	$5.3 \pm 0.5$	$2.8 \pm 0.1$	$0.20 \pm 0.14$	$5.9 \pm 0.2$	$-3.9 \pm 0.2$
18	$7.09 \pm 0.03$	$1.1 \pm 0.1$	$4.8 \pm 0.4$	$2.2 \pm 0.1$	$0.01 \pm 0.12$	$5.3 \pm 0.1$	$-3.6 \pm 0.2$
19	$5.42 \pm 0.01$	$2.7 \pm 0.1$	$7.9 \pm 0.5$	$4.6 \pm 0.1$	$-0.21 \pm 0.17$	$9.3 \pm 0.2$	$-4.6 \pm 0.2$
20	$5.73 \pm 0.01$	$2.6 \pm 0.1$	$8.3 \pm 0.2$	$4.4 \pm 0.1$	$-0.40 \pm 0.08$	$9.1 \pm 0.1$	$-4.3 \pm 0.1$
21	$6.77 \pm 0.02$	$1.9 \pm 0.1$	$6.4 \pm 0.3$	$3.3 \pm 0.1$	$-0.24 \pm 0.10$	$7.6 \pm 0.1$	$-3.7 \pm 0.1$
22	$4.57 \pm 0.01$	$2.8 \pm 0.1$	$10.8 \pm 0.4$	$4.6 \pm 0.1$	$-0.91 \pm 0.13$	$8.2 \pm 0.2$	$-5.6 \pm 0.2$
23	$4.82 \pm 0.01$	$2.0 \pm 0.1$	$9.5 \pm 0.5$	$4.0 \pm 0.0$	$-0.39 \pm 0.13$	$6.3 \pm 0.1$	$-5.3 \pm 0.2$
24	$5.19 \pm 0.03$	$2.0 \pm 0.2$	$7.7 \pm 1.7$	$2.9 \pm 0.2$	$-0.23 \pm 0.51$	$7.2 \pm 0.3$	$-4.6 \pm 0.8$
25	$4.50 \pm 0.01$	$3.1 \pm 0.1$	$9.1 \pm 0.6$	$5.2 \pm 0.1$	$-0.69 \pm 0.22$	$9.2 \pm 0.2$	$-5.1 \pm 0.4$

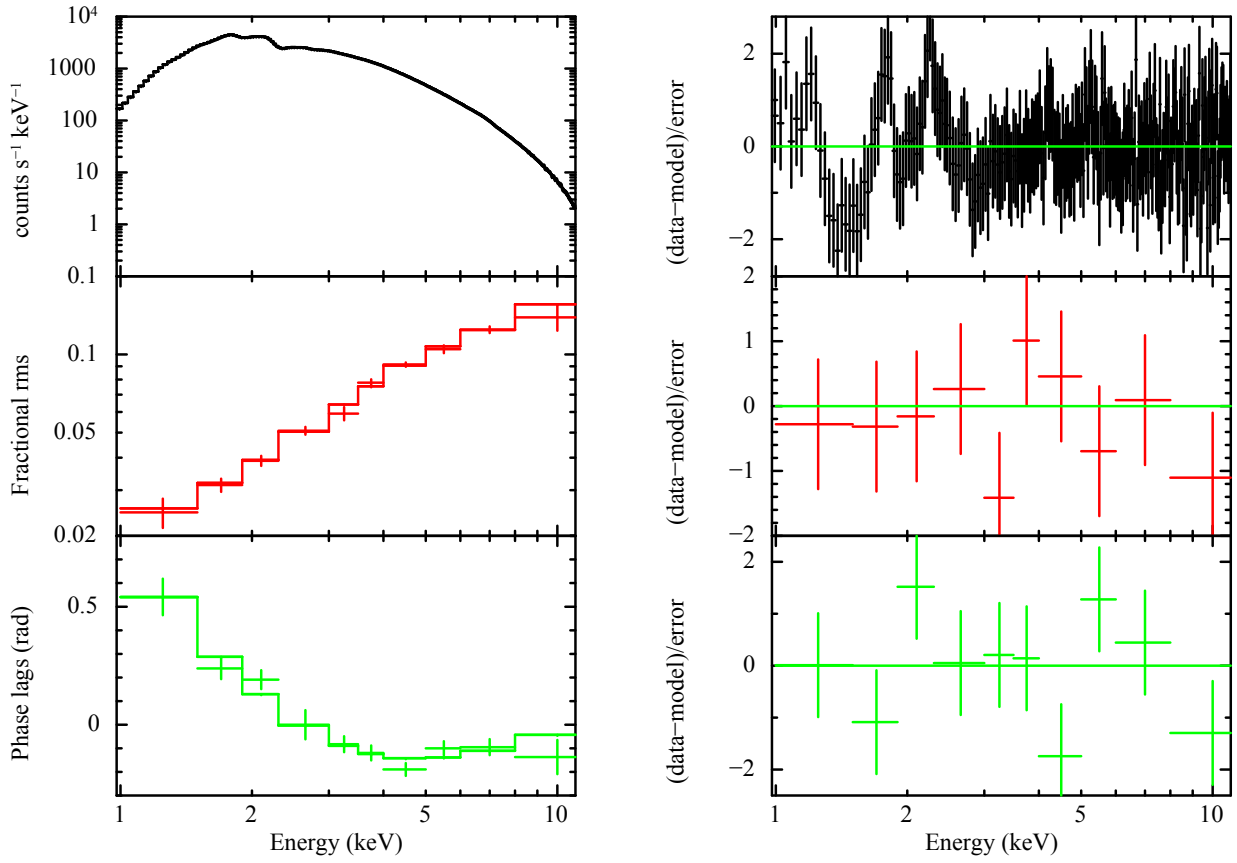


**Figure A2.** The same plot as shown in Figure 7 at  $\sim 4.5$  Hz QPO frequency in MAXI J1535–571.



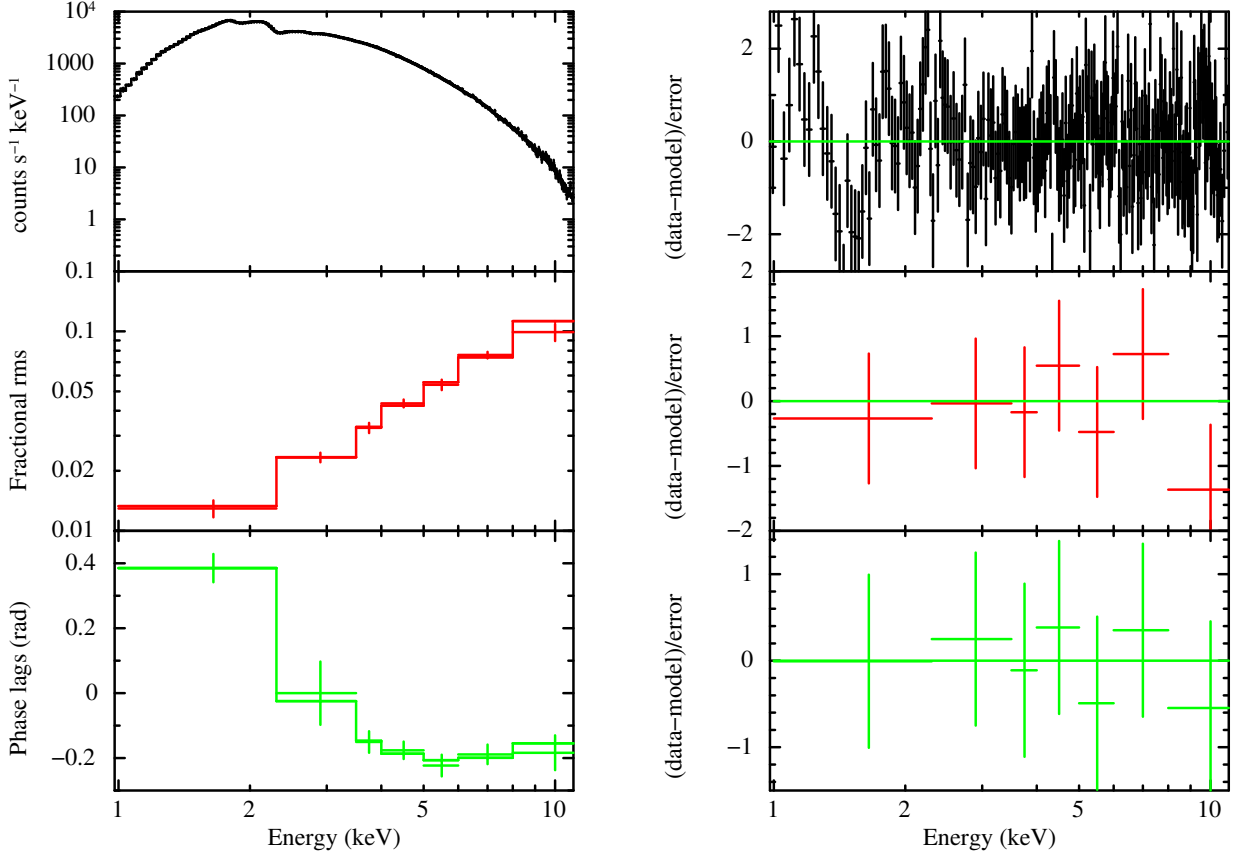


**Figure A3.** The same plot as shown in Figure 7 at  $\sim 7.0$  Hz QPO frequency in MAXI J1535–571.

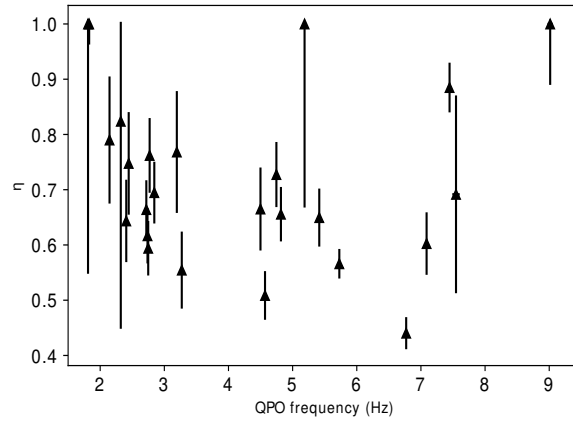


**Figure A4.** Dependence of the  $\eta$  upon QPO frequency in MAXI J1535–571. The values of  $\eta$  are obtained from the fits to the time-averaged spectra, the rms and phase-lag spectra of the QPO.